# NACA

RESEARCH MEMORANDUM

COMPARISON OF EXPERIMENTAL AND THEORETICAL ZERO-LIFT

WAVE-DRAG RESULTS FOR VARIOUS WING-BODY-TAIL

COMBINATIONS AT MACH NUMBERS UP TO 1.9

By Robert B. Petersen

Ames Aeronautical Laboratory
Moffett Field, Calif.

NATIONAL ADVISORY COMMITTEE
FOR AERONAUTICS
WASHINGTON
March 27, 1957

ERRATA

NACA RM A56I07

By Robert B. Petersen
March 27, 1957

Page 26, figure 2(e):

The wing area distribution presented is incorrect. The following table gives the correct increment in wing area above the body area distribution.

Body station x, in.	Wing area, in.^{2}
20.3	0
22	.72
24	1.97
26	3.35
28	4.55
30	5.38
31	5.60
32	5.65
33	5.53
34	5.22
36	4.02
38	1.56
39	0

Page 36, figure 8(b):

The theoretical zero-lift wave drag coefficients for $M = 1.0$ to $M = 1.5$ are too low. At $M = 1.0$ the value of ΔC_{D_O} should be 0.0087 and at $M = 1.50$ the value of ΔC_{D_O} should be 0.0056.

NATIONAL ADVISORY COMMITTEE FOR AERONAUTICS

RESEARCH MEMORANDUM

COMPARISON OF EXPERIMENTAL AND THEORETICAL ZERO-LIFT

WAVE-DRAG RESULTS FOR VARIOUS WING-BODY-TAIL

COMBINATIONS AT MACH NUMBERS UP TO 1.9

By Robert B. Petersen

SUMMARY

Comparisons are made of experimental and theoretical zero-lift wave drag for several nose shapes, wing-body combinations, and models of current airplanes at Mach numbers up to 1.9. The experimental data were obtained from tests in the Ames 6- by 6-foot supersonic wind tunnel and at the NACA Wallops Island facility. The theoretical drag was found by use of a linear theory utilizing model area distributions.

The agreement between theoretical and experimental zero-lift wave-drag coefficients was generally very good, especially for a fuselage or for fuselage-wing combinations that were vertically symmetrical. For other models that had rapid changes in body shape and/or were not vertically symmetrical, the agreement of theory with experiment ranged from fair to poor, depending on the severity of the change in shape.

INTRODUCTION

In reference 1 a method was suggested for estimating the zero-lift wave drag of wing-body combinations moving at supersonic speeds. The mechanics of applying this method were developed in references 2 and 3. These references also presented some comparisons between experiment and theory at speeds near the speed of sound. The investigation reported herein was undertaken to provide similar comparisons for other models, namely several nose shapes, wing-body combinations, and current airplanes, for Mach numbers up to 1.9. A concurrent study reported in reference 4 provides further comparisons between experiment and theory for nose shapes, wings, and wing-body combinations. Such comparisons indicate some of the limitations of this theory in predicting the zero-lift wave drag of a system of wings and bodies traveling at supersonic speeds.
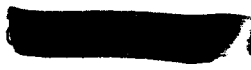
SYMBOLS

A_n dimensionless coefficients defining the magnitude of the harmonics of the Fourier sine series

C_{D_O} zero-lift drag coefficient, $\dfrac{\text{zero-lift drag}}{qS_D}$

C_F average skin-friction coefficient, $\dfrac{\text{average skin-friction drag}}{q(\text{wetted area})}$

ΔC_{D_O} zero-lift wave drag, $\dfrac{\text{zero-lift wave drag}}{qS_D}$

l length of equivalent body

M free-stream Mach number

N number of terms or harmonics used in the Fourier sine series

n a harmonic of the Fourier sine series

q free-stream dynamic pressure

R Reynolds number

S projection of area in oblique cutting planes onto a plane parallel to the yz plane

$S'(x)$ first derivative of S with respect to x

$S''(x)$ second derivative of S with respect to x

S_D area upon which drag coefficients are based (see table I)

V free-stream velocity

x,y,z Cartesian coordinates
(Origin is at nose and positive x,y,z directions are rearward and parallel to body axis, starboard, and upwards, respectively.)

θ angle between the positive z axis and the intersection of a plane tangent to the Mach cone with the yz plane (positive angles counterclockwise from positive z axis looking upstream)

μ Mach angle, $\arcsin \dfrac{1}{M}$

ρ mass density of air

ψ angle between the positive y axis and the intersection of the oblique cutting planes with the xy plane, arc tan (cot μ cos θ) (positive angles clockwise from y axis looking down)

MODELS AND TEST

The configurations studied in the present report were two nose shapes, several bodies, wing-body combinations, and current airplanes and are shown in figure 1. The normal cross-sectional area distributions, modified where necessary to produce zero slope at the nose and the tail, are shown in figure 2. This modification is required by the theory used herein and will be discussed at a later point in this report.

The nose shapes, models A and B, were parts of complete models fired from the helium gun at the NACA Pilotless Research Station, Wallops Island, Virginia. The complete models consisted of the nose shape having a fineness ratio of 3 to 1 and an afterbody which was identical in each case. The afterbody comprised a cylindrical section of fineness ratio 4 to 1 followed by a conical section of fineness ratio 5 to 1. Three fins were mounted on the aft end of the conical section.

The drag forces for models A and B were obtained from the deceleration history of the model as it traveled along a ballistic trajectory. The data were obtained for a range of Mach numbers from 0.8 to 1.25 for Reynolds numbers between 5.3 and 10 million per foot. The drag coefficients presented herein are based on the maximum cross-sectional area of the body (table I) and were estimated to be accurate to ±0.008.

Models C to I shown in figure 1 were investigated in the Ames 6- by 6-foot supersonic wind tunnel. Models C and D had the same distribution of cross-sectional area and differed only in the shape of the cross section, model C having circular cross sections and model D having cross sections more nearly rectangular. Models F and I had protuberances on the side of the fuselage which approximated the fuselage shape with ducts having inlets faired closed. On models G and H the air inlets were open. The models were sting-mounted in the wind tunnel and the forces were measured with an internal electrical strain-gage balance.

The data for models C to I were obtained at Mach numbers between 0.60 and 0.93 and between 1.20 and 1.90. The Reynolds number was 3 million per foot for models C, D, E, F and H, 1.5 million per foot for model G, and 4 million per foot for models E less wing and I. The drag coefficients presented herein for these models were based on an assumed wing area for models C and D and the total wing area for models F through I. The drag coefficients have been corrected for model base pressure drag by adjusting the pressure over the base to correspond to the free-stream static-pressure curve. The drag coefficients are considered to be accurate to ±0.0005.
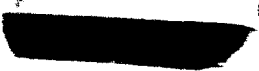
THEORETICAL CALCULATIONS

Reference 1 relates the zero-lift wave drag of a configuration, composed of wings and bodies, traveling at a supersonic speed to the average drag of a certain group of equivalent bodies of revolution. The determination of the area distribution of the equivalent bodies of revolution is discussed in the Appendix. It suffices to say here that the area distribution for each equivalent body is related to that of the real system of wings and bodies by so-called cutting planes which are inclined at the Mach angle to and a roll angle about the longitudinal or x axis of the system. The group of equivalent bodies of revolution comprises all such bodies for roll angles of the cutting planes from $0°$ to $360°$.

The drag for each of the equivalent bodies of revolution can be computed from von Kármán's formula for the wave drag of a slender body of revolution,

$$D'(\theta) = \frac{\rho V^2}{4\pi} \int_{-l/2}^{l/2} \int_{-l/2}^{l/2} S''(x)S''(x_1)\log(x - x_1)dx \, dx_1$$

This equation can be simplified to

$$D'(\theta) = \frac{\pi \rho V^2}{8} \sum nAn^2$$

when $S'(x)$ is expanded in a Fourier sine series (see ref. 5). To permit the expansion of $S'(x)$ in a Fourier sine series, it is necessary that the value of $S'(x)$ be zero at the nose and tail of the body. The total drag of the wing-body system is then found from

$$D = \frac{1}{2\pi} \int_0^{2\pi} D'(\theta)d\theta$$

This equation can be further simplified to

$$D = \frac{1}{\pi} \int_{-\pi/2}^{\pi/2} D'(\theta)d\theta$$

for wing-body systems which have a vertical plane of symmetry.

The area distributions for the configurations studied herein were found by a graphical procedure which is explained in some detail in the Appendix. Five area distributions for different roll angles between $-\pi/2$ and $\pi/2$ were determined for all of the configurations investigated herein except for those models which were bodies of revolution. A typical group of such area distributions as obtained from the areas intersected by a series of cutting planes at a Mach angle of $41.8°$ ($M = 1.5$) is shown in figure 3(a) for model F less tail. For models G and H the area distributions found by the methods given in the Appendix were modified to take account of the area of the ducts. The modification consisted in subtracting from the total area distribution the area of the duct which was taken as a straight-line variation from the inlet area to the exit area. The treatment of the duct area in this fashion simulates a mass-flow ratio of 1 through the duct (see ref. 3).

After the area distributions were found for the equivalent bodies of revolution, the coefficients A_n in the Fourier sine series expressing $S'(x)$ were determined. The quantity $\sum nA_n^2$ was then calculated and plotted with respect to roll angle as shown in figure 3(b). The average value of $\sum nA_n^2$ for insertion in the drag equations was then found graphically from such plots.

It is noted that a smooth curve has been drawn through the five points in figure 3(b) corresponding to the five equivalent bodies of revolution which were evaluated. However, for those values of θ in which the cutting planes are parallel to a round leading or trailing edge of a wing or tail there is a sudden change in area distribution at the value of x where the plane intersects the edge of the wing or tail, thereby producing an infinite slope, $S'(x)$, and therefore, an infinite value of $\sum nA_n^2$.

The linear theory used herein would no longer be valid under such circumstances since it would indicate an infinite wave drag. Since experimental results have indicated no large values of drag which would be associated with these infinite values of $\sum nA_n^2$ in the theoretical calculations, no attempt has been made in this report to define such values in the plots such as figure 3(b). Furthermore, in the evaluation of $\sum nA_n^2$ only 24 or 25 A_n terms were used in the Fourier sine series defining $S'(x)$.
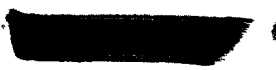
The area distributions for the five roll angles, $\pm\frac{\pi}{2}$, $\pm\frac{\pi}{4}$, and 0, and hence the drag, were obtained at Mach numbers of 1.0, 1.4, and 1.8 for models A and B and at Mach numbers of 1.0, 1.5, and 1.9 for models C to I. For models A, B, and E the coefficients A_n were determined by expanding the slope of the area distribution in a Fourier series using harmonic analysis as in reference 2. For the other models, the coefficients A_n were found by an improved method (ref. 3) in which Tchebichef polynomials are substituted into the equations defining the coefficients of the Fourier series.

CALCULATION OF EXPERIMENTAL WAVE DRAG

Models A and B

The experimental zero-lift drag coefficients (C_{D_0}) for models A and B which are presented in reference 6 are shown in figures 4(a) and 5(a). As described in reference 6, the zero-lift wave drag for each of the nose sections (figs. 4(b) and 5(b)) was obtained by subtracting from the zero-lift drag data of the nose-afterbody-fin combination the friction drag of the combination, the wave drag of the afterbody and fins, and the base pressure drag. The friction drag of the combination was estimated by a method of Van Driest in which the boundary-layer flow is assumed to be completely turbulent, an assumption considered in reference 6 to be valid. The base pressure drag and the wave drag of the afterbody and fins were determined from the difference between the base pressure and wave drag of an identical afterbody and fin in combination with a cone-shaped nose and the wave drag of the cone-shaped nose alone as determined theoretically. It is assumed in determining the base pressure and wave drag in this manner that the pressure fields of various nose shapes do not significantly affect the pressure drag of the afterbody and fins. This assumption appears justifiable since the forward portion of the afterbody is a fineness-ratio-4 cylinder.

Models C Through I

The experimental zero-lift drag for models C through I are shown in figures 6 through 16. The zero-lift wave drag coefficient for most of these models was obtained by subtracting the estimated friction drag from the measured zero-lift drag coefficient.

Generally, in the past the zero-lift wave drag has been found by subtracting the zero-lift drag at subsonic speeds, usually considered to be the friction drag, from the total zero-lift drag at supersonic speeds. This method in effect assumes that the friction drag is independent of

of Mach number, an assumption essentially valid if the boundary layer on the entire surface is laminar. A portion of the boundary layer is turbulent, however, and the results of reference 7 show that the friction drag coefficient for a turbulent boundary layer varies with Mach number. In the present calculations, therefore, that portion of the zero-lift drag at supersonic speeds considered to result from a turbulent boundary-layer flow was corrected for the effects of Mach number according to the factor presented in reference 7. The magnitude of the experimental skin-friction drag coefficient resulting from the turbulent boundary-layer flow was estimated from a comparison of the experimental zero-lift drag at 0.8 Mach number and calculated values of the skin-friction drag for completely laminar and completely turbulent boundary-layer flow. The following equation gives the estimated value for the skin-friction drag coefficient on the model at any Mach number.

$$C_{D_F} = \frac{E - L}{T - L} \, T \, \frac{C_F}{C_{F_{M=0.8}}} + \frac{T - E}{T - L} \, L$$

Most of the symbols in this equation can best be described in the following illustration.
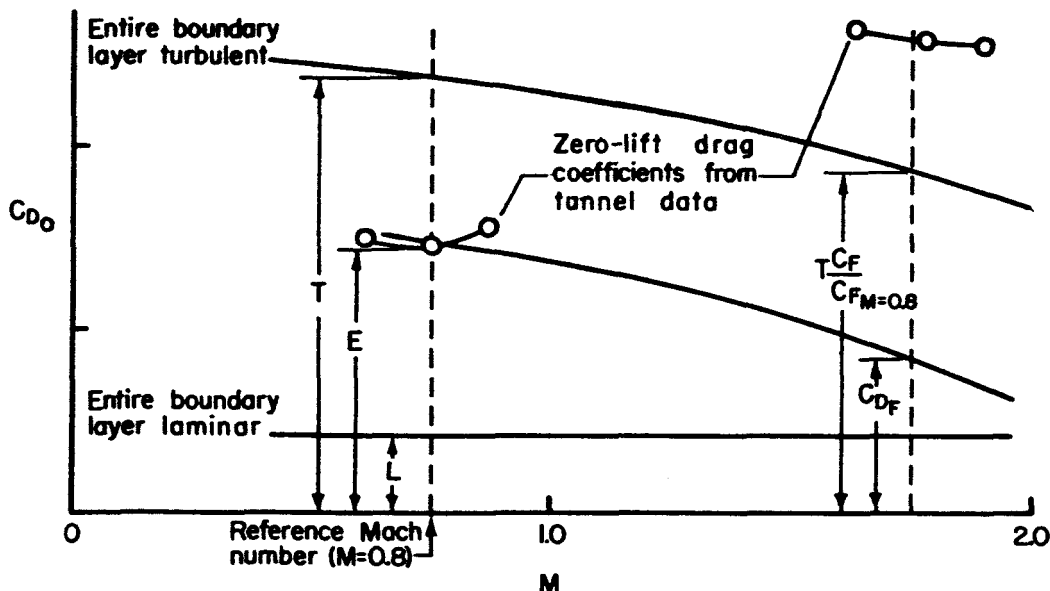
The ratio $\dfrac{C_F}{C_{F_{M=0.8}}}$ is the friction drag coefficient at some Mach number to the friction drag coefficient at a Mach number of 0.8 for a model where

all its area is in turbulent flow (see ref. 7). The equation is valid
if the boundary-layer transition point does not change with Mach number,
which is the assumption made in this report.

The skin-friction drag for a model was computed by estimating the
drag of each model component and then adding the drag of all the com-
ponents together. The skin-friction drag of the body in which the entire
boundary layer is turbulent was found by using the results of figure 15
in reference 7. The skin-friction drag coefficient for fully laminar
flow was found from the equation $C_F = 1.33/\sqrt{R}$ as derived in refer-
ence 8. As mentioned previously, the slight variation in C_F with Mach
number was neglected for the laminar case. The Reynolds number used in
calculations for both types of boundary-layer flow was based on the
over-all length for the body and on the mean aerodynamic chord for a wing
or tail surface.

The drag data for models F, G, G less tail, and H (figs. 10, 13, 14,
and 15) contain drag caused by sources other than friction which must be
considered in calculating the zero-lift wave drag. The drag due to lift
of the horizontal tail of model F was estimated from tail-on and tail-off
data of the model to be approximately 0.0003 at subsonic speeds and about
0.0013 at supersonic speeds, and these values were used in calculating
the wave drag for that model. The wing of model G is cambered, resulting
in an increment of drag at zero lift which was estimated from 6- by 6-foot
supersonic wind tunnel data for wings of similar plan form with and with-
out camber to be about 0.0017 at subsonic speeds and about 0.0023 at
supersonic speeds. This drag due to camber and an additional drag due
to lift of various components were taken into account in the calculations
of the wave drag. In computing the wave drag for models G and H the
internal drag of the ducts has been subtracted.

RESULTS AND DISCUSSION

A comparison of the theoretical zero-lift wave drag and the experi-
mental data for models considered herein are presented in figures 4
through 16 inclusive. As might be expected for the range of Mach numbers
and models considered, the agreement ranged from poor to very good. In
general, agreement was poor at transonic speeds as evidenced by the results
for models A and B in figures 4 and 5. This lack of agreement is as
expected because the theory used herein is a linear theory which shows
the transonic drag rise as a step at $M = 1.0$, and it is well known that
experiment does not show this step.

In general, the agreement between experimental and calculated values
of zero-lift wave drag for Mach numbers above approximately 1.2 was very
good for vertically symmetrical fuselages alone or with thin symmetrical
wings mounted on them. For example, the comparison of data for models A,
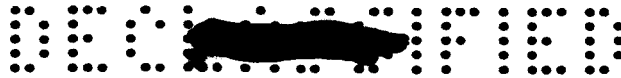
B, C, E, E less wing, and F less tail (figs. 4, 5, 6, 8, 9, and 11), gener-
ally shows very good agreement. However, within this group of models
having vertically symmetrical fuselages there were several cases in which
the agreement was poor, namely the results for model F less the wing, tail,
and duct fairing protuberances (fig. 12) at most of the Mach numbers, and
for model E (fig. 8) and model F less the tail (fig. 11) at a Mach number
of 1.9. In the case of model F less the wing, tail, and duct fairings,
the discrepancy between experiment and theory has not been explained.
In the case of the discrepancies at M = 1.9, there are indications that
the data may be faulty. It will be noted that for some of the models the
experimental values of C_{D_0} at M = 1.9 are considerably above the values
at the lower supersonic Mach numbers. Models E and F less tail are very
dissimilar so that one would not suspect a configuration characteristic
to be responsible for the rise in C_{D_0} at a Mach number of 1.9. However,
both sets of results were obtained in the Ames 6- by 6-foot wind tunnel
wherein severe pressure disturbances are known to exist in the empty test
section at a Mach number of 1.9. Such pressure disturbances may be
responsible for the apparently faulty experimental data at this mach number.

Two sources of disagreement of the theoretical zero-lift wave drag
with experimental data noted for the models considered are believed to
be a lack of vertical symmetry and/or a rapid variation of shape. For
models C and D, which had the same area distribution in planes perpendicu-
lar to a body axis, there was good agreement for model C but poorer agree-
ment for model D. This is attributed to the fact that model D did not
have vertical symmetry. Model I, in addition to lack of vertical symmetry,
had the most rapid variation of shape of any of the models considered and
showed very poor agreement. A probable explanation of the lack of agree-
ment for models D and I is suggested by reference 9. Lomax shows in this
report that when the shape of the body is such to cause a nonsymmetrical
pressure distribution and, hence, a resultant pressure force in the planes
of some of the oblique area cuts, then the theoretical zero-lift wave drag
is different from that calculated by the method used herein.

A comparison of theoretical and experimental ΔC_{D_0} for models F
and G shows agreement which is not as good as the comparison for these
models without the tail. It is noted that the removal of the high vertical
tail of model G actually increases the estimated value of ΔC_{D_0} at the
highest test Mach number. This increase can be attributed to the fact
that the length of the equivalent body of revolution at a roll angle (θ)
of $-\pi/2$ is shorter and hence the area distribution is more blunt near
the aft end for model G less tail than for the complete model. As
expected, the theory predicts a higher wave drag for this blunt body
than for the less blunt body representing the configuration with the
vertical tail.

CONCLUSIONS

A comparison of the theoretical zero-lift wave drag and the experimental data for several aerodynamic bodies indicates the following general conclusions:

1. The agreement of theory with experiment was poor near transonic Mach numbers. This lack of agreement arises because the linear theory used predicts a step at a Mach number of 1.0 which is not characteristic of experimental data.

2. The agreement above transonic speeds was very good for vertically symmetrical fuselages alone or in combination with a symmetrical wing.

3. The agreement above transonic speeds for two fuselages with similar area distributions showed poorer agreement for the one which did not have vertical symmetry.

4. The agreement above transonic speeds for a model with a rapid and nonsymmetrical change in shape was very poor.

Ames Aeronautical Laboratory
    National Advisory Committee for Aeronautics
        Moffett Field, Calif., Sept. 7, 1956

APPENDIX

DETERMINATION OF AREA DISTRIBUTIONS OF

EQUIVALENT BODIES OF REVOLUTION

According to the theory used in this report, the zero-lift wave drag
of a particular aerodynamic configuration is dependent upon the area dis-
tribution of a series of bodies, each of which is related to the geometry
of the configuration. To find the perpendicular cross-sectional area
distribution of one of these bodies, imagine the configuration with
a series of Mach planes spaced along its length and at the same roll angle
around the x axis with respect to its z axis. Each Mach plane slicing
through the configuration defines a certain area. This area and similar
areas for other x positions projected onto a plane perpendicular to the
x axis defines the desired area distribution. By repeating the above
process for other roll angles between 0° and 360°, one obtains the desired
area distributions of a series of equivalent bodies.

Area distributions used herein were found by a graphical procedure
using three-dimensional geometry. Although other graphical methods for
finding these area distributions are available, the present method is
discussed in some detail to indicate the degree of accuracy of the area
distributions used herein.

AREA DISTRIBUTION OF A FUSELAGE

To find the area distributions which depend only on the fuselage,
contour maps are constructed which represent the shape of the side of the
fuselage as observed from a position perpendicular to the x axis and at
an angle of θ from the positive z axis. The construction of a contour
map is illustrated in figure 17(a). For this simple example the fuselage
is a cylinder, symmetrical about the xz plane, and a roll angle of 90°
has been selected for the viewing position. As a result of symmetry,
the contour map at a roll angle of 270° $(\theta + 180^{\circ})$ is the same as that
for a roll angle of 90° and hence is not required. To construct the
contour map, contour planes were used. The edge view of these contour
planes which are perpendicular to the line of sight (parallel to the xz
plane for this particular viewing position) are shown on the top view of
the model. The contour map shows lines which represent the intersection
of these contour planes with the body surface. Each of these lines is a
constant distance from the vertical plane of symmetry and this distance
is noted on the contour map. The location of one point on one of these
lines is found by intersecting the periphery of a typical section, such
as AA in figure 17(a), by a line which represents a contour plane. Two
such points are shown projected onto the contour map at station x_1.

Connecting these points to those of the same elevation at nearby stations, such as x_2, gives contour lines which for the illustration model are straight since the body has a constant section.

After the contour map is constructed, for the roll angle of 90°, the area intersected by a Mach plane at a roll angle of 90° can be obtained as in figure 17(b). As shown, the line representing the edge view of the Mach plane at a roll angle of 90° is drawn on the contour map intersecting the x axis at the desired value of x and at an angle of μ to the x axis. At each point where this Mach plane line intersects a contour line, the distance from the fuselage surface to the plane passing through the x axis and perpendicular to the line of sight is known. This distance is laid off perpendicular to the cutting line and establishes one point on the periphery of the cut. Connecting this point and similar points for other contour lines gives the dotted line representing the area inter- sected on one side of the fuselage by a Mach plane at a roll angle of 90°. As indicated, the construction can be done either on the contour map or offset as in section CC. In the present case because of the assumed symmetry, the area can be doubled to get the total area intersected. However, in the general case it is necessary to repeat this operation on the contour map for $\theta + 180^O$ to obtain the total intersected area. This area is then multiplied by sine μ to obtain the area projected onto the plane perpendicular to the x axis. The area intersected by the Mach plane at a roll angle of $\theta + 180^O$, in the present case 270°, is determined in a fashion similar to that discussed for a roll angle of 90° except that the cutting line is drawn at an angle of $-\mu$ to the x axis. As before, the area is multiplied by sine μ to obtain the area projected onto the plane perpendicular to the x axis.

Use of the contour map in determining the fuselage area intersected by the Mach plane at a roll angle of $\theta \pm 90^O$, in the present case 180° and 0°, is illustrated in figure 17(c). The dotted vertical lines on the contour map represent the intersection of Mach planes at $\theta \pm 90^O$ and the contour planes. The location of these vertical lines can be determined either graphically or mathematically. To determine the spacing graphi- cally a view of the fuselage at an angle $\theta - 90^O$ is drawn as in the upper part of figure 17(c). On this view, lines parallel to the x axis are drawn which represent the edge view of the contour planes. Lines repre- senting the edge view of the Mach planes at roll angles of both $\theta - 90^O$ and $\theta + 90^O$ are then drawn through the appropriate value of x on the x axis and at an angle of $+\mu$ and $-\mu$ with respect to the x axis. The intersections of these Mach planes with the contour planes are projected onto the contour map giving the required spacing of the vertical lines on the contour map. The spacing of these lines can also be readily deter- mined mathematically since the spacing between the contour planes and the angle of the Mach planes, μ, are known. Dividing the distance between two contour planes by tangent μ gives the desired x distance between the lines of intersection of the contour planes and the Mach plane. The locus of the points of intersection of the contour lines with the vertical

lines in the contour planes gives the projection of the area in the Mach plane onto the contour plane through the x axis. In the present case because of fuselage symmetry, the complete area can be obtained from the single contour map as in figure 17(c). However, in the general case of the cut at the roll angle $(\theta - 90°)$, that portion to the right of the vertical line in the contour plane through the x axis would have to be obtained from the contour map of the opposite side of the fuselage. For the cut at the roll angle $(\theta + 90°)$ the portion on the left side would have to be obtained from the contour map of the opposite side. Multiplying the total area by tangent μ gives the projection of the area on the plane perpendicular to the x axis.

The example discussed above is a specialized case where a contour map of a body symmetrical about the xz plane was developed for a viewing direction of $\theta = 90°$. Due to the model symmetry about the xz plane it was shown that the area cut by the Mach plane at the roll angle of $(\theta - 90°)$ is the same as that cut by the angle $(\theta + 90°)$ when $\theta = 90°$. This similarity in the area cut by two different Mach planes can be further explained by a more general approach. For instance, if the fuselage is symmetrical about a plane which contains the x axis and is at a roll angle γ about the x axis from the positive z axis, then the Mach planes on either side of the plane at roll angles of θ and $180° + 2\gamma - \theta$ will have a common line of intersection in the plane of symmetry and will intersect an equal area on the fuselage. Here again, if the plane of symmetry is the xz plane then $\gamma = 0$ and the area cut at a roll angle of θ is the same as that for a roll angle of $180° - \theta$.

Now if a fuselage has a plane of symmetry it can be shown using the general rule just derived that eight area distributions representing eight different roll angles can be found by carefully choosing a pair of contour maps. For example, assume that the roll angle for the contour plots is $30°$ and $210°$. It is always possible then, using the methods discussed previously, to find the area distributions for roll angles $30°$, $120°$, $210°$, and $300°$. If the fuselage is symmetrical about the xz plane, these area distributions are the same as those at roll angles $150°$, $60°$, $-30°$ $(330°)$ and $-120°$ $(240°)$, respectively.

AREA DISTRIBUTION OF A WING

The graphical layout for finding the area distribution of a wing is shown in figure 18. The first step in making the layout is to compute the ordinates of the wing along constant-percent-chord lines. Figure 18 shows two constant-percent-chord lines and corresponding lines on the wing surface representing the perpendicular distance of the wing surface above the chord plane.
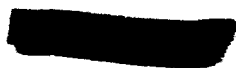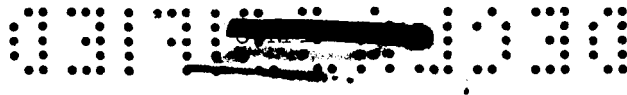
Since the wing is thin, the cutting planes can be taken perpendicular to the wing-chord plane without introducing a significant error in area. The angle ψ at which the wing is cut is related to the roll angle θ, and to the Mach angle, μ, by the equation

$$\psi = \text{arc tan } (\cot \mu \cos \theta)$$

At each point where this cutting plane intersects the constant-percent-chord line the ordinate of the wing is known. This ordinate is laid off perpendicular to the cutting plane, thus determining one point on the periphery of the wing cut. Connecting the points from all the constant-percent-chord lines indicates the upper surface of the wing cut. If the wing is symmetrical then the integrated area between the surface and the line in the chord plane gives half of the area in interest at a particular station. This area must be doubled and added to the area of a similar cut at $-\psi$ for the opposite wing panel. This area is then multiplied by $\cos \psi$ and added to the area of the body at a station position where the cutting plane intersects the reference body axis.

REFERENCES

1. Jones, Robert T.: Theory of Wing-Body Drag at Supersonic Speeds.
   NACA RM A53H18a, 1953.

2. Holdaway, George H.: Comparison of Theoretical and Experimental Zero-
   Lift Drag-Rise Characteristics of Wing-Body-Tail Combinations Near
   the Speed of Sound. NACA RM A53H17, 1953.

3. Holdaway, George H., and Mersman, William A.: Application of
   Tchebichef Form of Harmonic Analysis to the Calculation of Zero-Lift
   Wave Drag of Wing-Body-Tail Combinations. NACA RM A55J28, 1956.

4. Nelson, Robert L., and Welsh, Clement J.: Some Examples of the
   Applications of the Transonic and Supersonic Area Rules to the
   Prediction of Wave Drag. NACA RM L56D11, 1956.

5. Sears, William R.: On Projectiles of Minimum Wave Drag. Quart. Appl.
   Math., vol. IV, no. 4, Jan. 1947, pp. 361-366.

6. Stoney, William E., Jr.: Transonic Drag Measurements of Eight Body-
   Nose Shapes. NACA RM L53K17, 1954.

7. Chapman, Dean R., and Kester, Robert H.: Turbulent Boundary-Layer
   and Skin-Friction Measurements in Axial Flow Along Cylinders at
   Mach Numbers Between 0.5 and 3.6. NACA TN 3097, 1954.

8. Von Mises, Richard: Theory of Flight. McGraw-Hill Book Co., Inc.,
   1945.

9. Lomax, Harvard: The Wave Drag of Arbitrary Configurations in Linear-
   ized Flow as Determined by Areas and Forces in Oblique Planes.
   NACA RM A55A18, 1955.

TABLE I.- AREAS UPON WHICH DRAG COEFFICIENTS ARE BASED

Model	Area, S_D, sq ft	
A	0.01226	Maximum body cross-sectional area.
B	0.01226	
C	2.400	Arbitrary wing area.
D	2.400	
E	2.425	Gross wing area.
F	1.406	
G	5.338	
H	2.730	
I	1.626	

$$\frac{r}{r_0} = \frac{2\left(\frac{x}{x_0}\right) - K\left(\frac{x}{x_0}\right)^2}{2 - K}$$

$r_0 = .75$

x

r

$K = 1.0$

$x_0 = 4.5$

(a)   Model   A

All dimensions in inches

$$\frac{r}{r_0} = \frac{2\left(\frac{x}{x_0}\right) - K\left(\frac{x}{x_0}\right)^2}{2 - K}$$

$r_0 = .75$

x

r

$K = 0.75$

$x_0 = 4.5$

(b)   Model   B
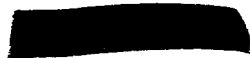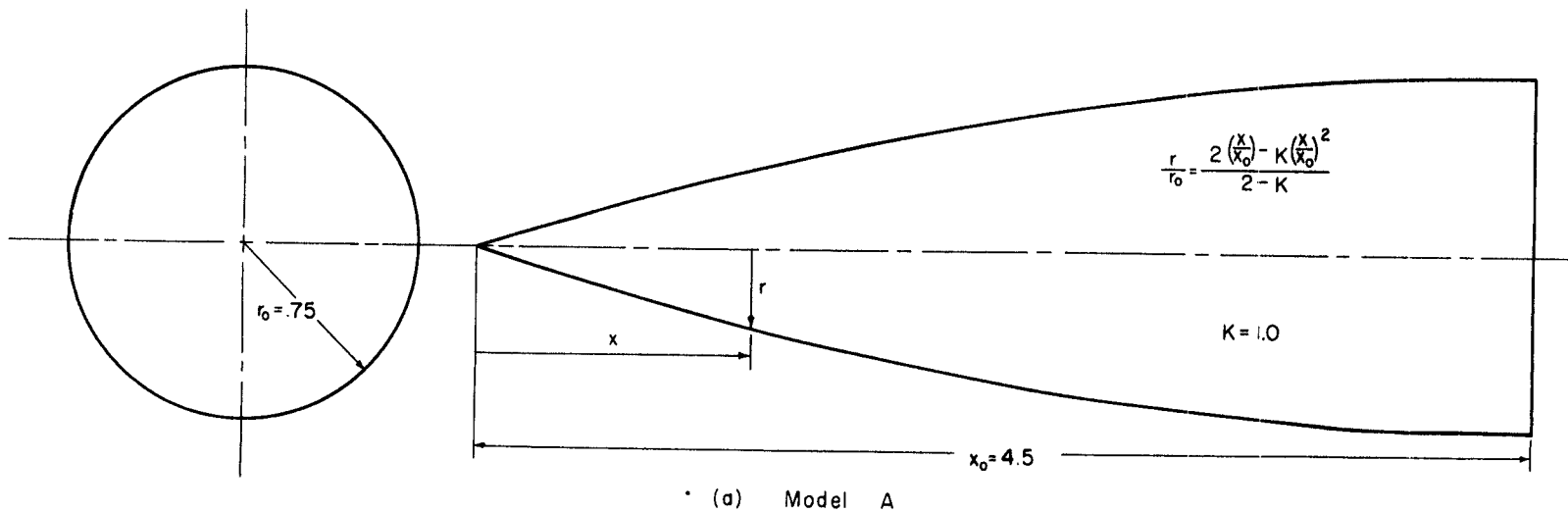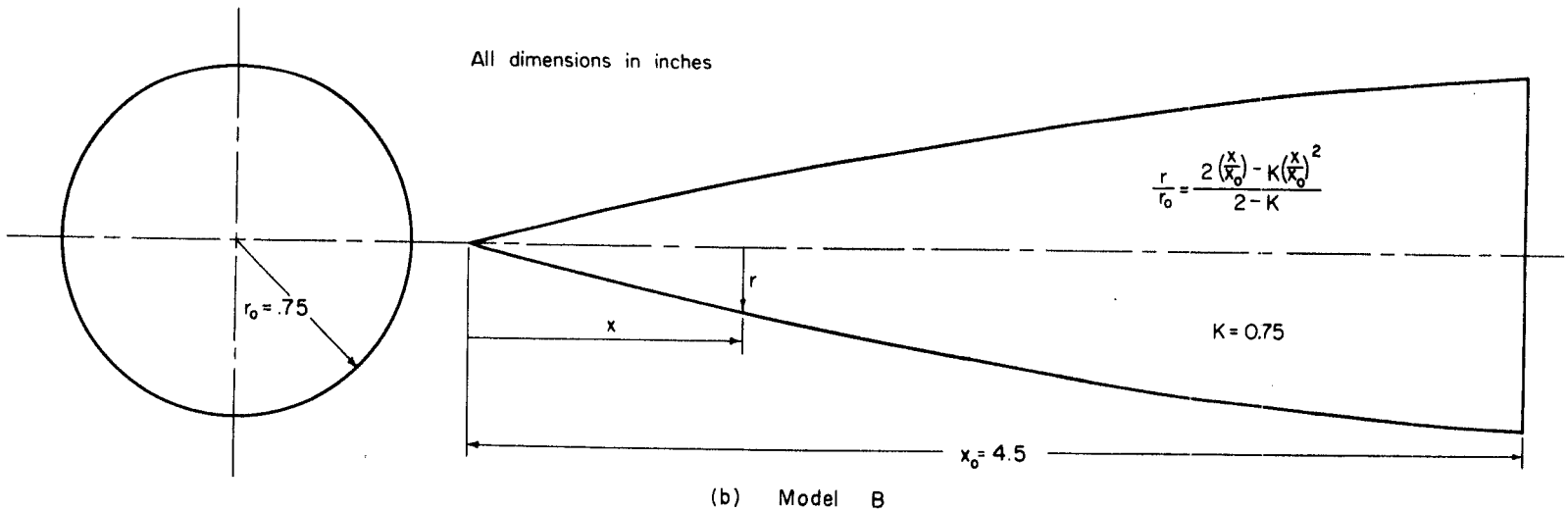
Figure 1.- Dimensional sketches of test models.

r=1.07
r=2.47

48.37

(c)   Model   C

4.61

4.88

48.37

All dimensions in inches

(d)   Model   D

Figure 1.- Continued.

All dimensions in inches

$r_0 = 2.38$

53.1°

17.32

21.58

8.03

$l = 59.50$

Wing airfoil section

NACA 0003-63

Body equation

$$\frac{r}{r_0} = \left[1 - \left(1 - \frac{2x}{l} \right)^2 \right]^{3/4}$$

32.38
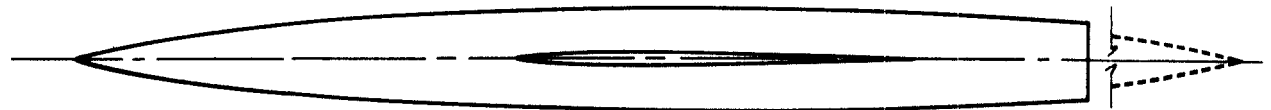
(e)   Model   E

Figure 1.- Continued.

43.48

22.50

23.41

Wing airfoil section
Front 0.5c elliptical
Rear 0.5c circular arc
Thickness ratio 3.4
percent

Vertical tail airfoil section
Root 4.5 percent biconvex with
leading-edge modification
Tip 5.25 percent biconvex with
leading-edge modification

27.1°

5.00

13.00

12.00

2.04

6.26

5°

4.47

43.75°

7.13

35.49

45.39

12.13

All dimensions in inches
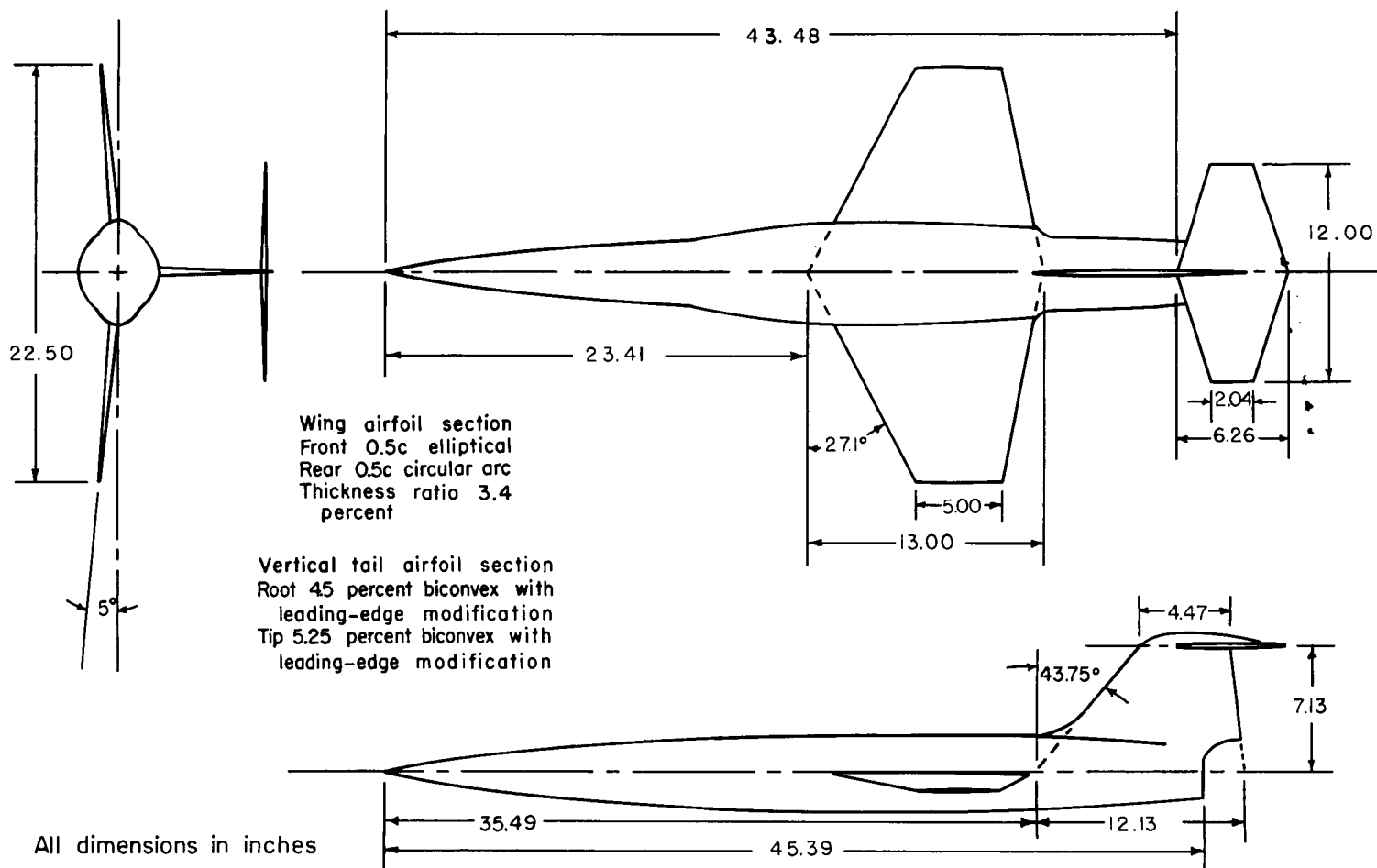
(f)   Model F

Figure 1.- Continued.

All dimensions in inches

15.29

8.59

40.14

15.77

60°

2.35

10°

19.15

34.77

38.31

61.71
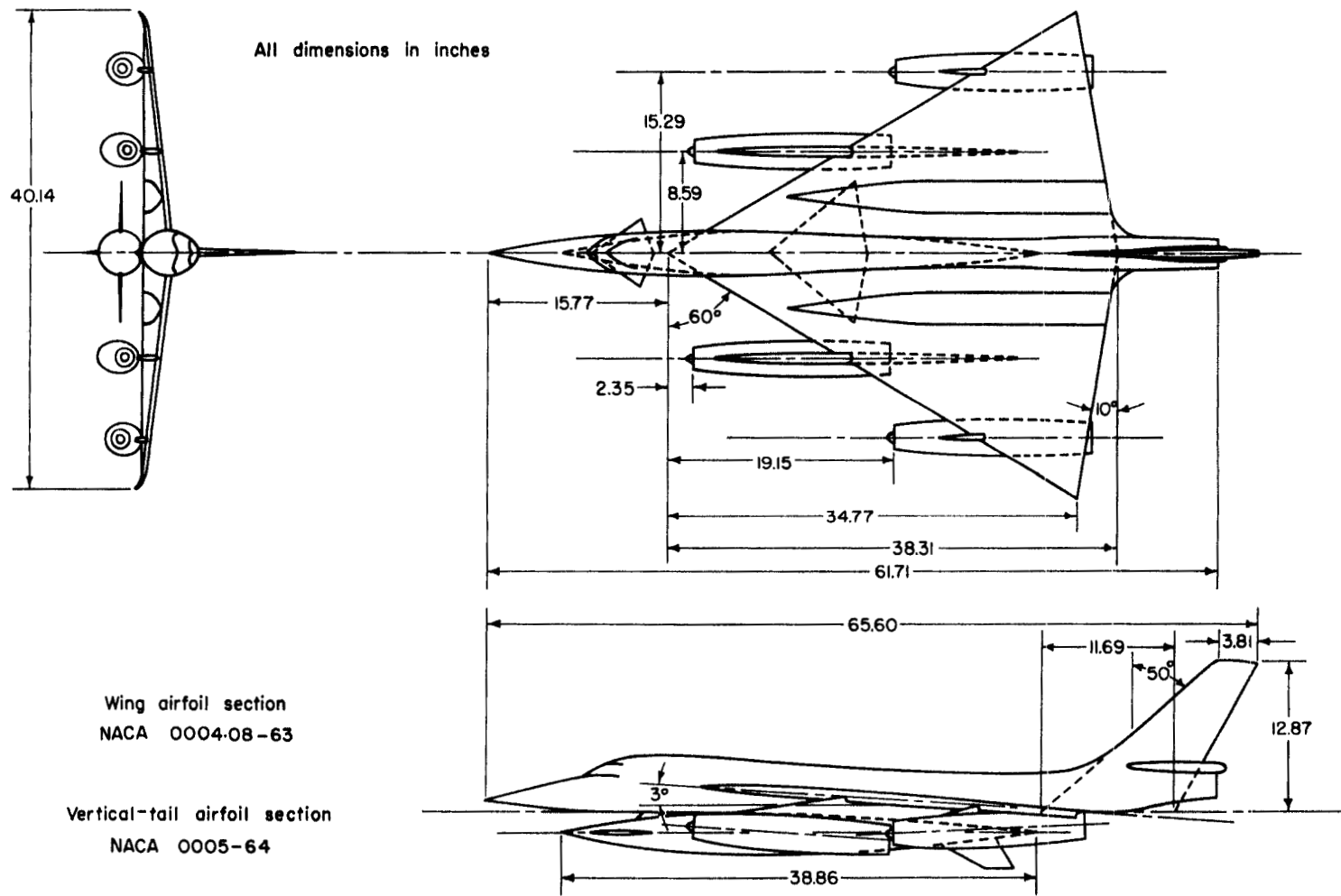
Wing airfoil section
NACA 0004.08-63

Vertical-tail airfoil section
NACA 0005-64

65.60

11.69

3.81

50°

12.87

3°

38.86

(g)   Model   G

Figure 1.- Continued.

28.16

21.08

13.00

Wing airfoil section
Root NACA 0007-63
Tip NACA 0004.5-63

Vertical-tail airfoil section
Root NACA 0008-63
Tip NACA 0006-63

Both wing and tail sections
modified to increase thickness
over rear portions

52.5°

9.90

7.00

3.92

52.5°

9.94

All dimensions in inches

28.22

39.34

9.84
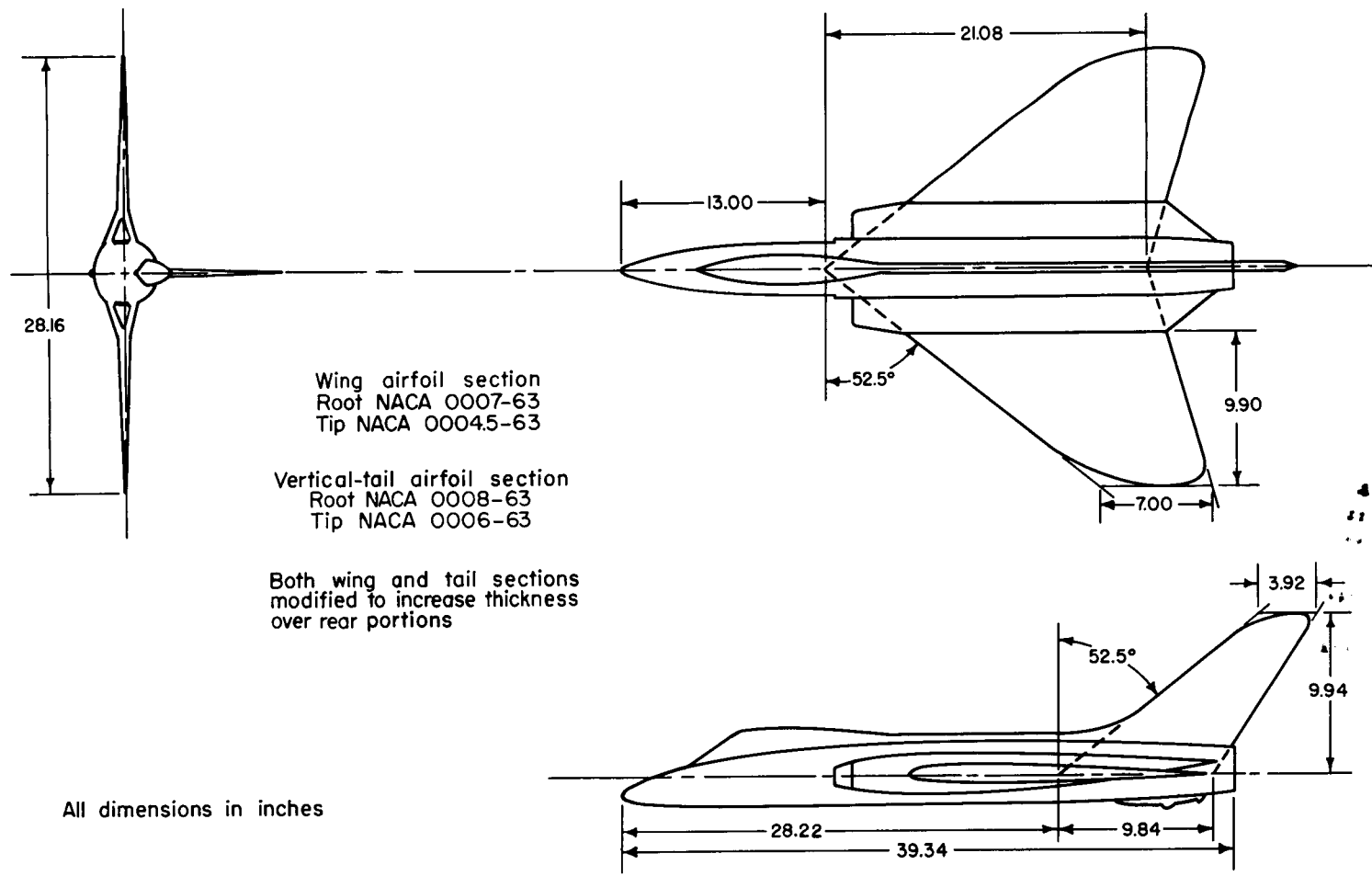
(h) Model H

Figure 1.- Continued.

All dimensions in inches
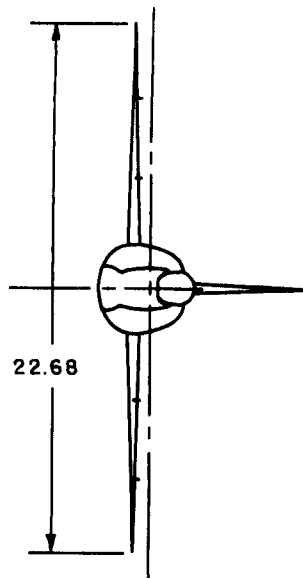
22.68

Wing airfoil section
NACA 0004-65

Vertical-tail airfoil section
NACA 0004-65

60°

10.423

20.630

32.886

11.785

60°

6.785

19.461

12.300

31.761
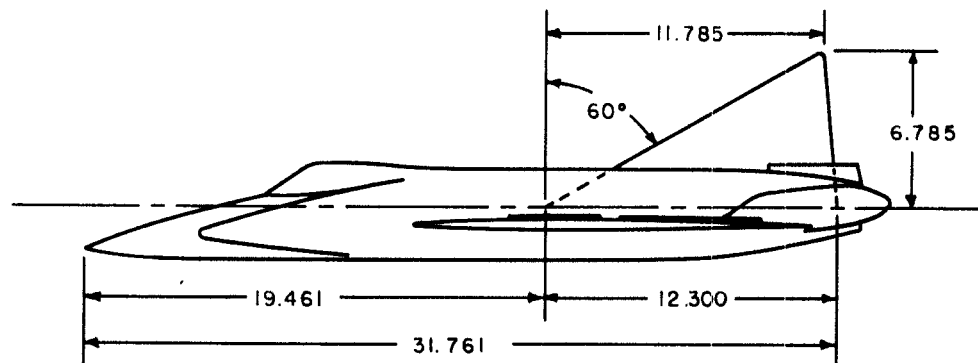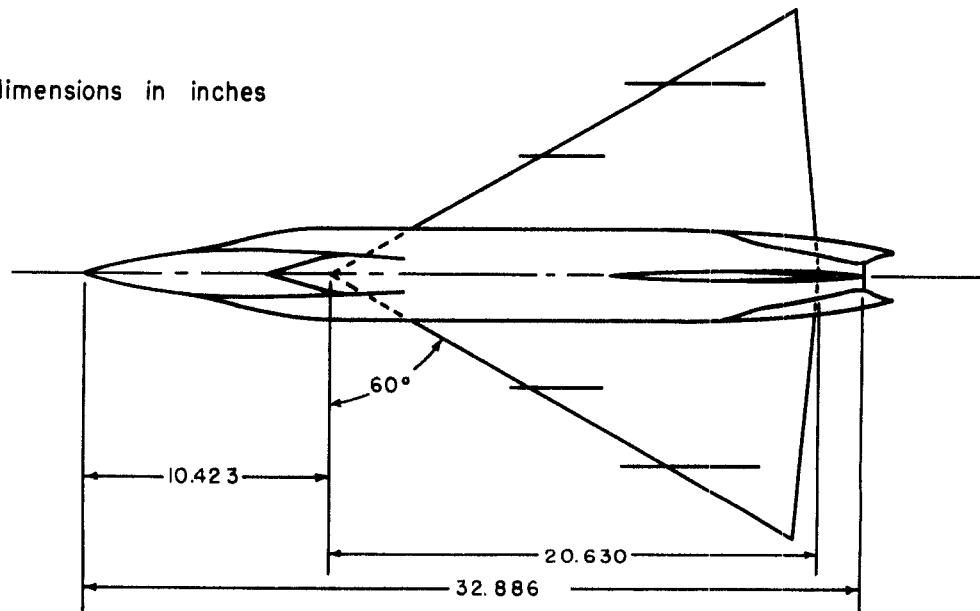
(i) Model I

Figure 1.- Concluded.
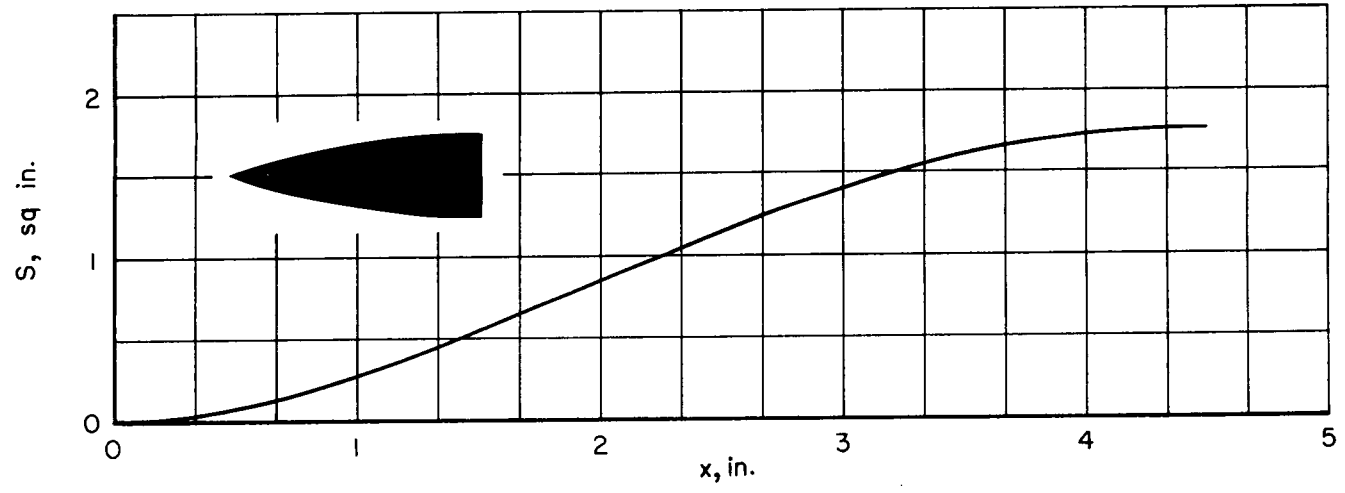
(a) Model A
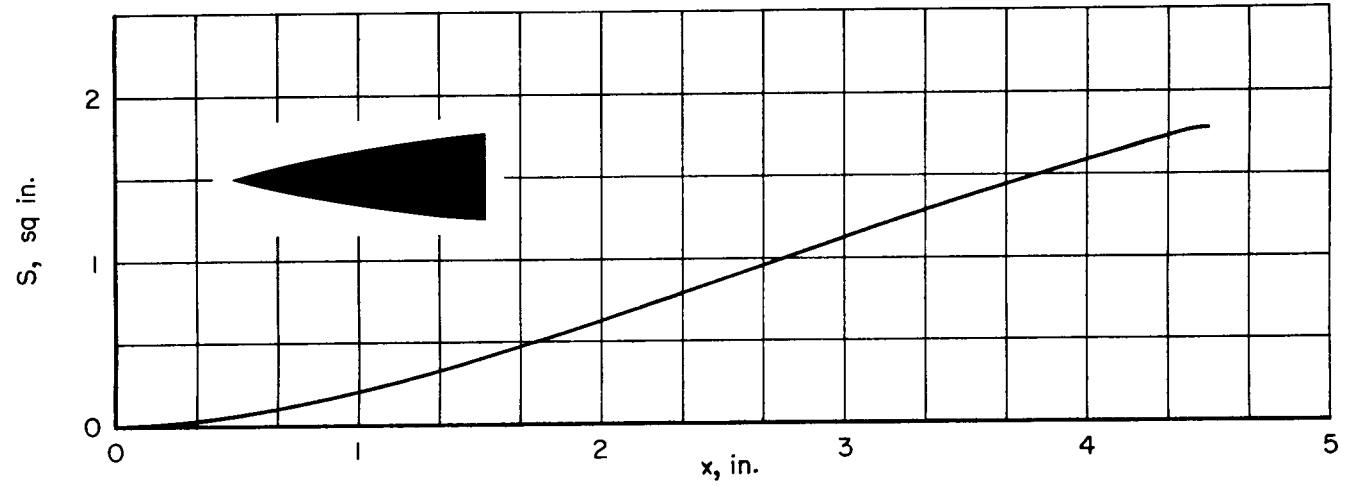
(b) Model B

Figure 2.- Normal cross-sectional-area distributions of the test models.
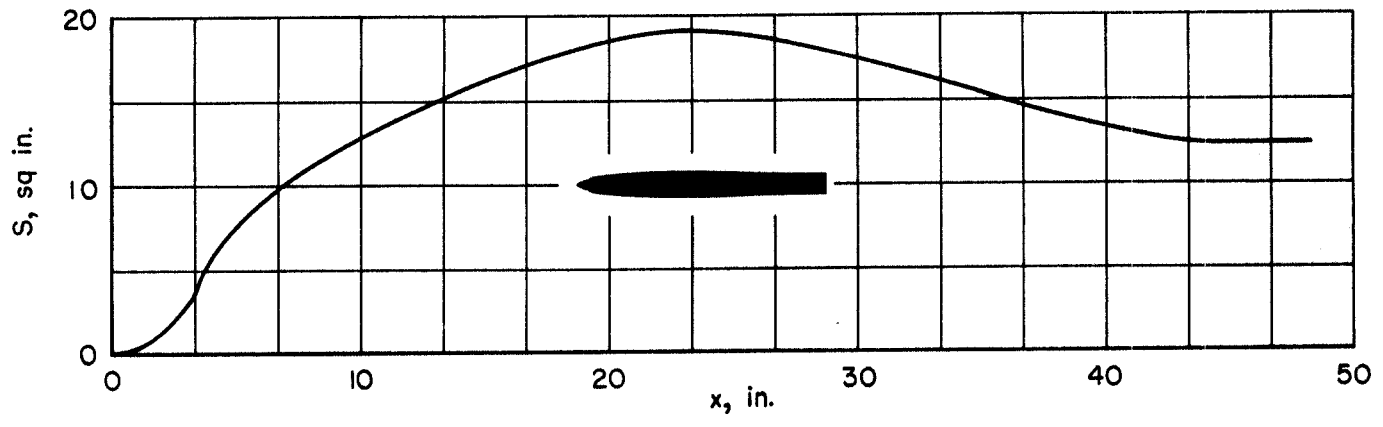
(c) Model C
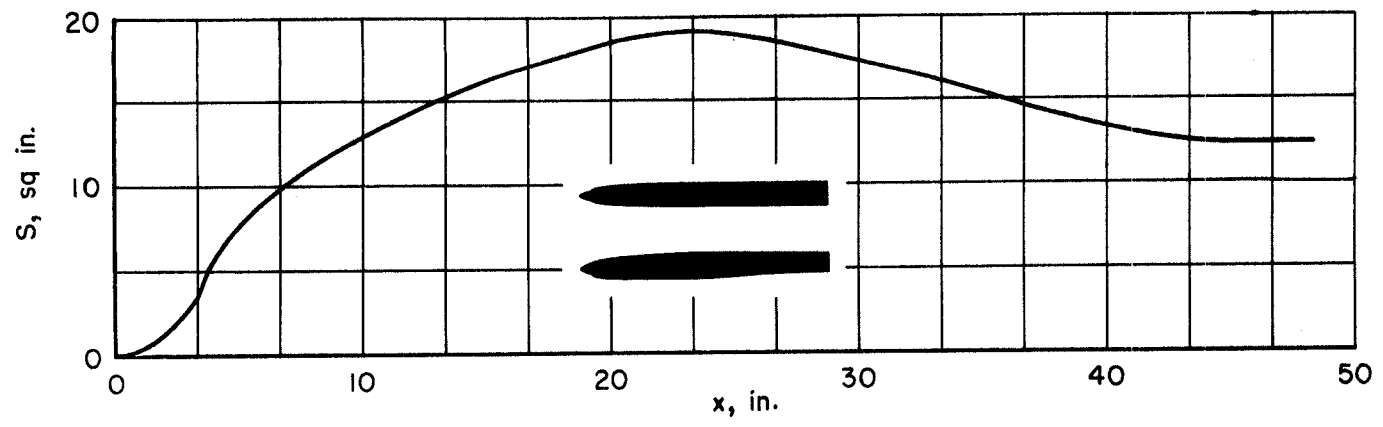
(d) Model D

Figure 2.- Continued.
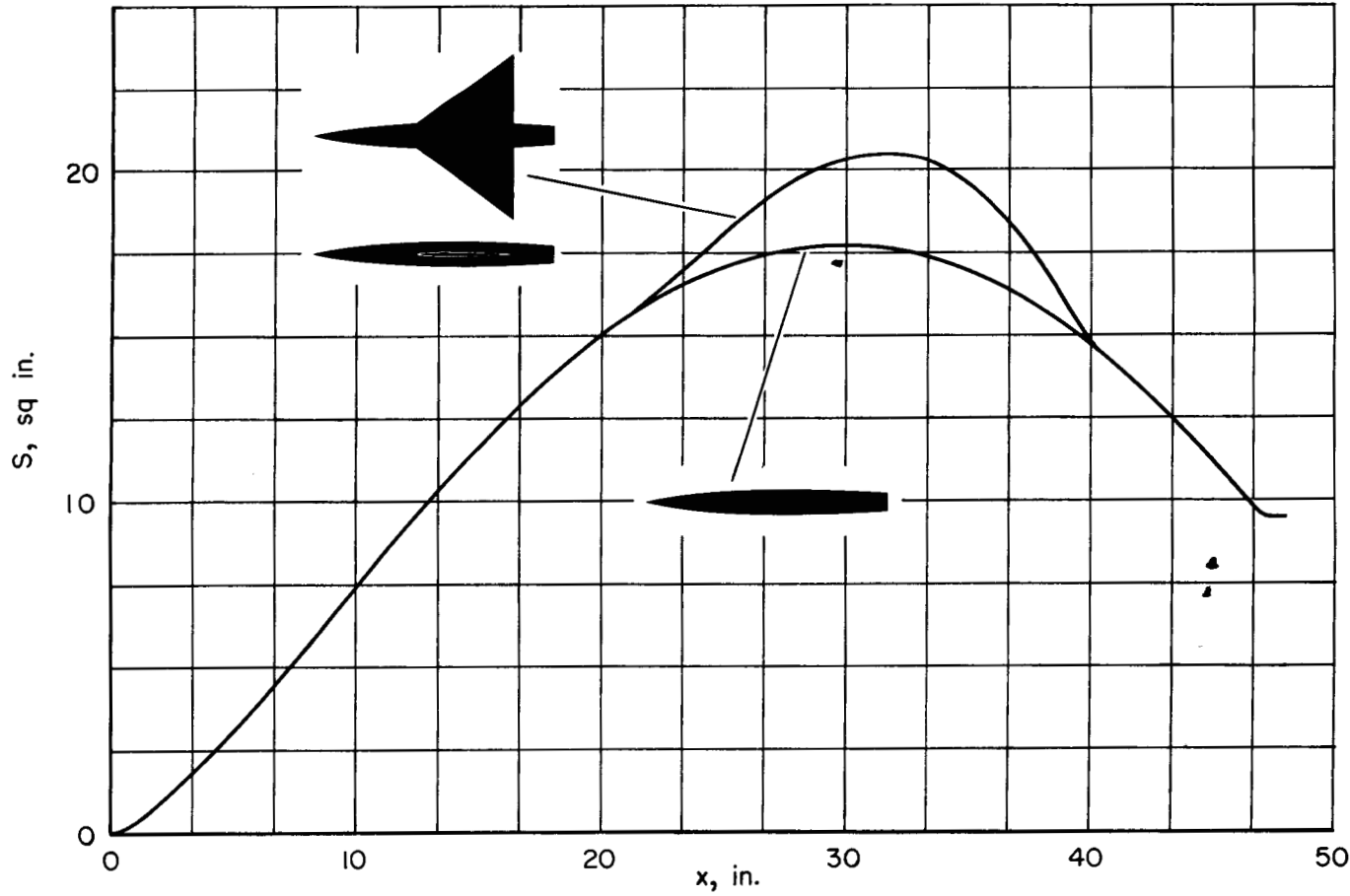
(e) Model E, and E less wing

Figure 2.- Continued.
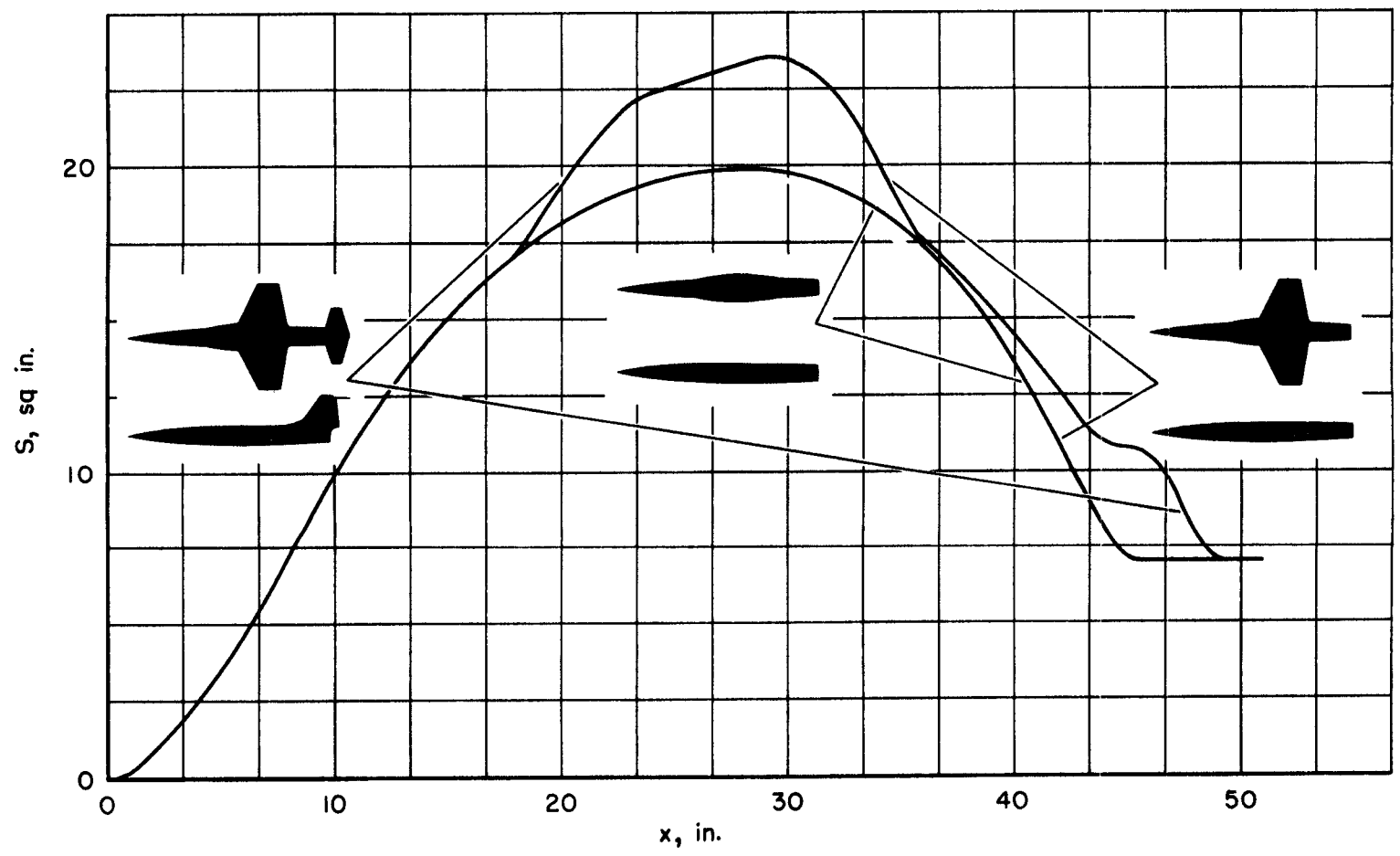
(f) Model F, F less tail, and F less wing and tail and ducts

Figure 2.- Continued.
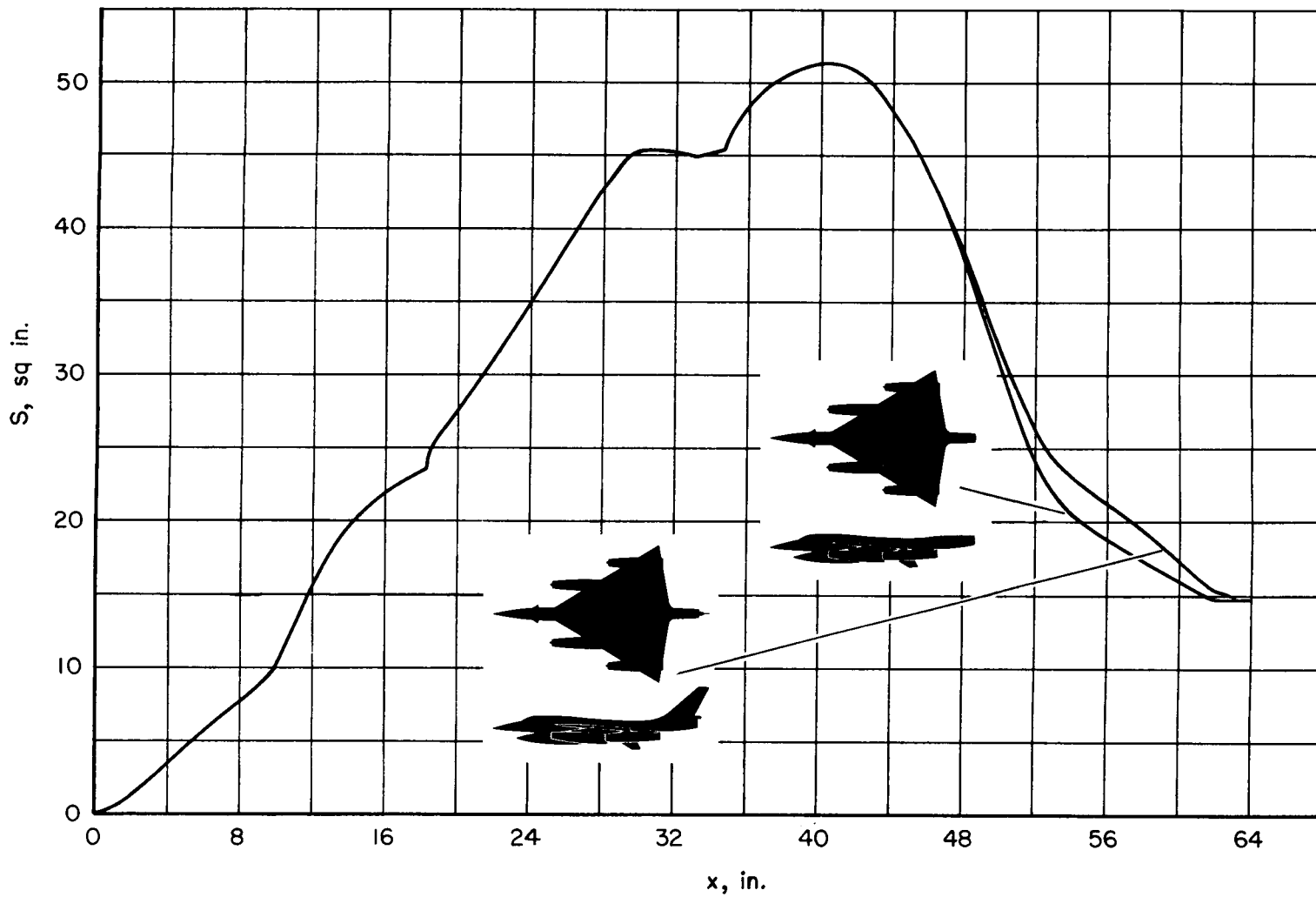
(g) Model G, and G less tail

Figure 2.- Continued.
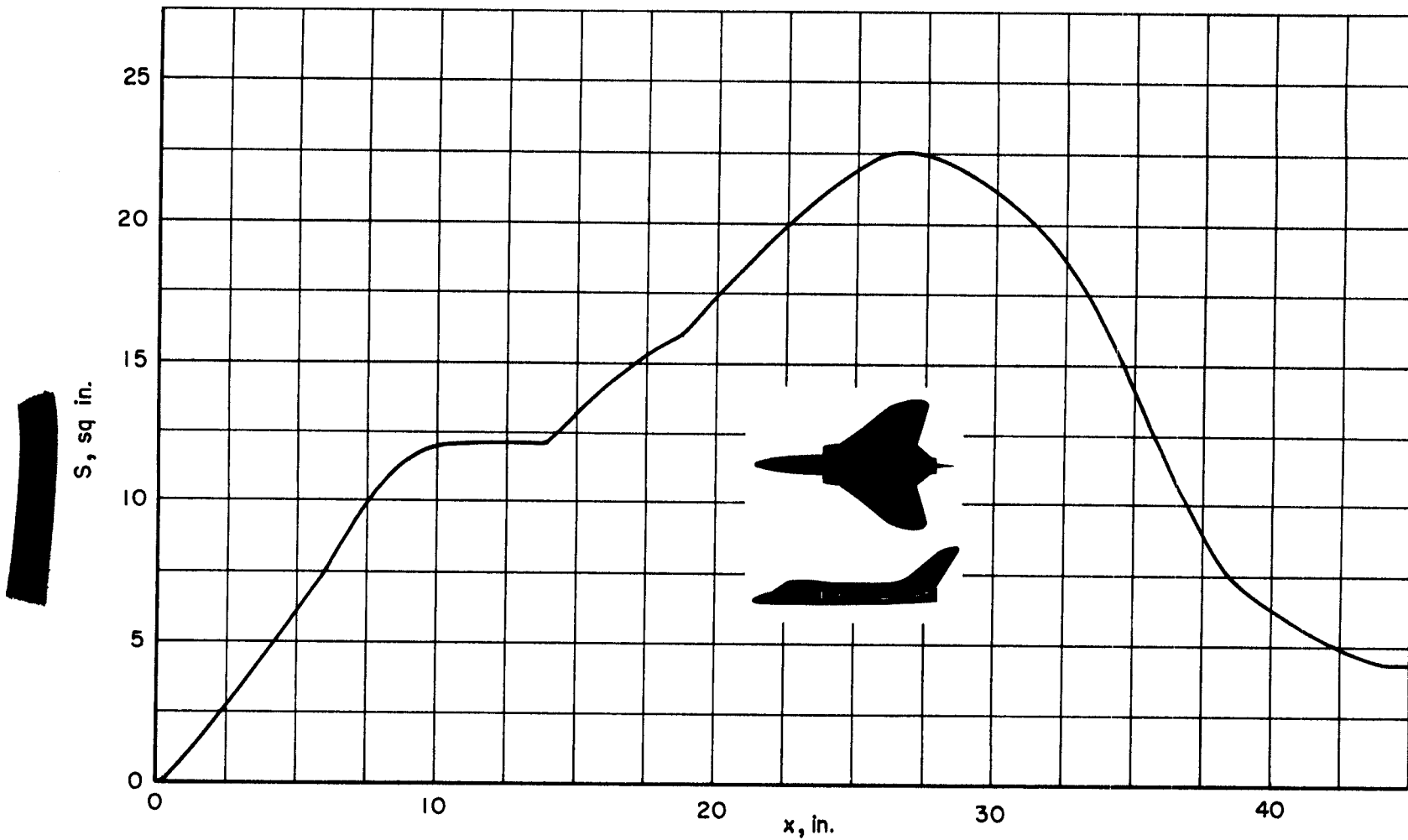
(h) Model H

Figure 2.- Continued.
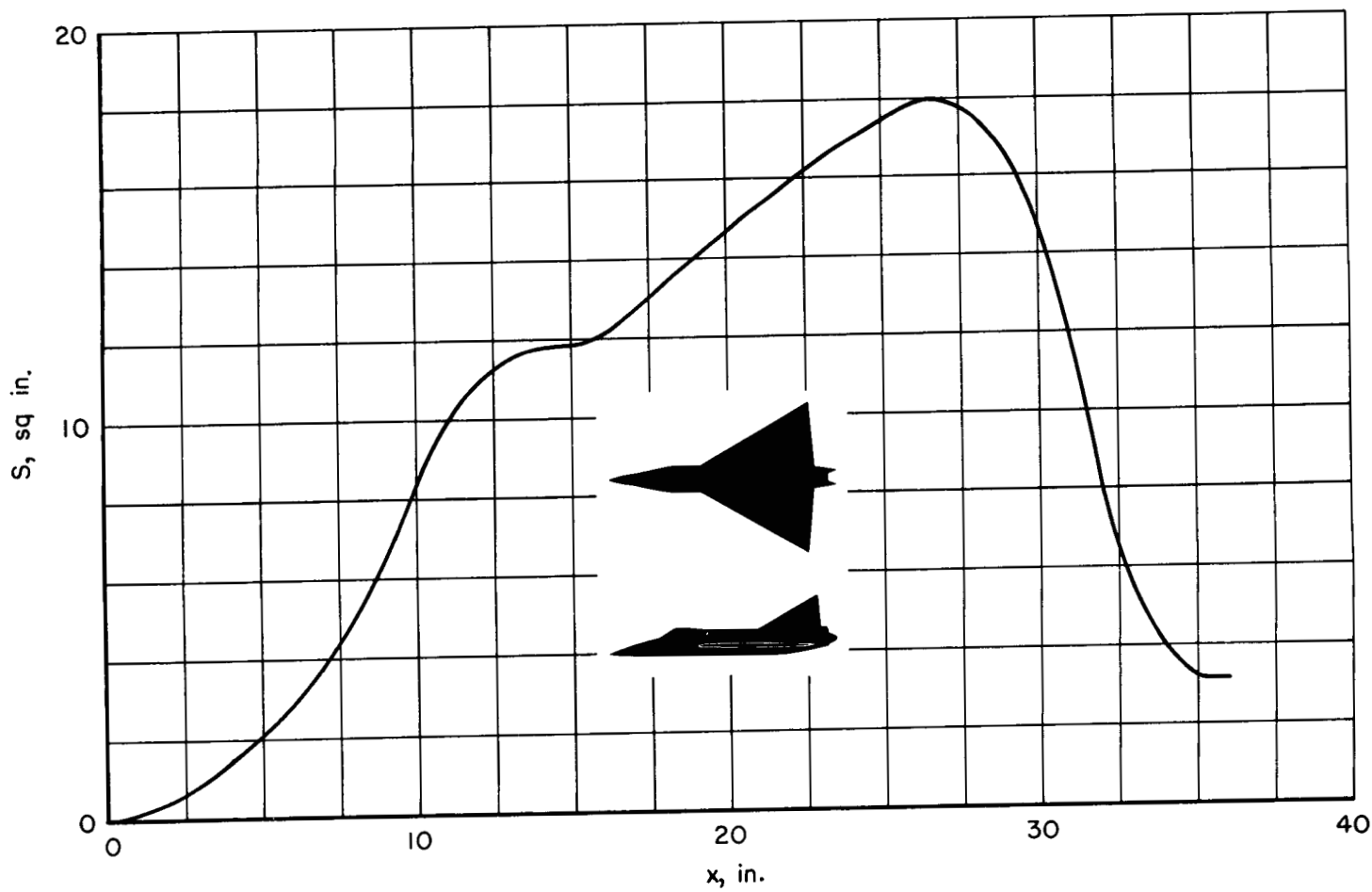
(i) Model I

Figure 2.- Concluded.

DECLASSIFIED
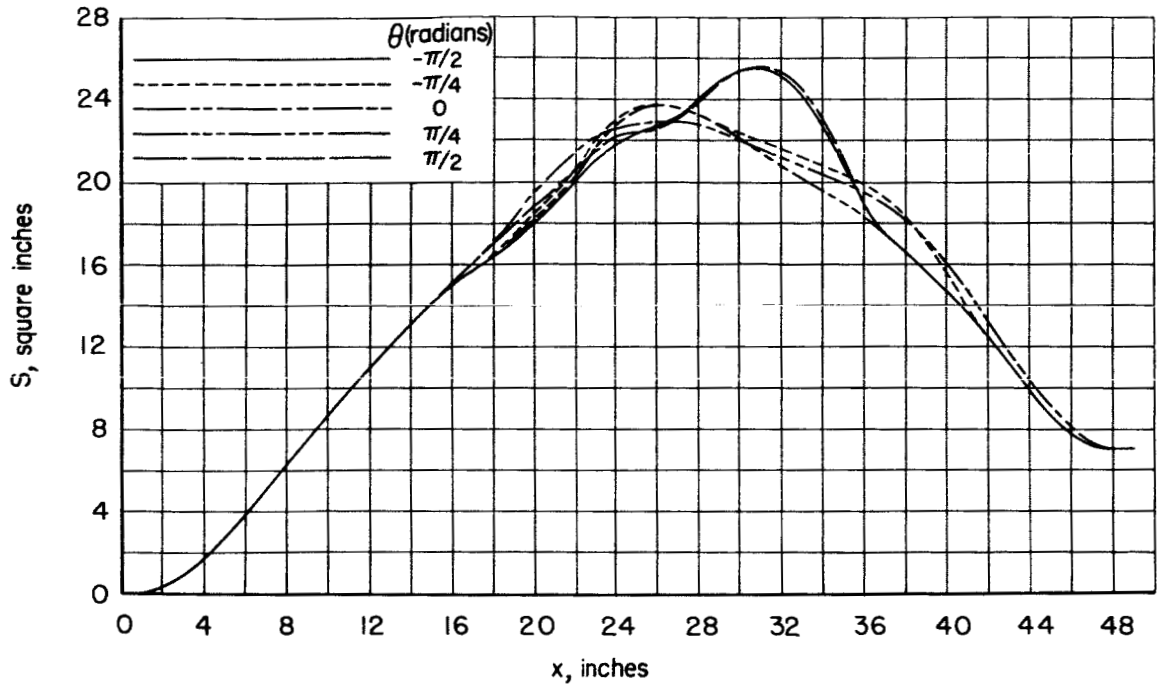
(a) S vs. x
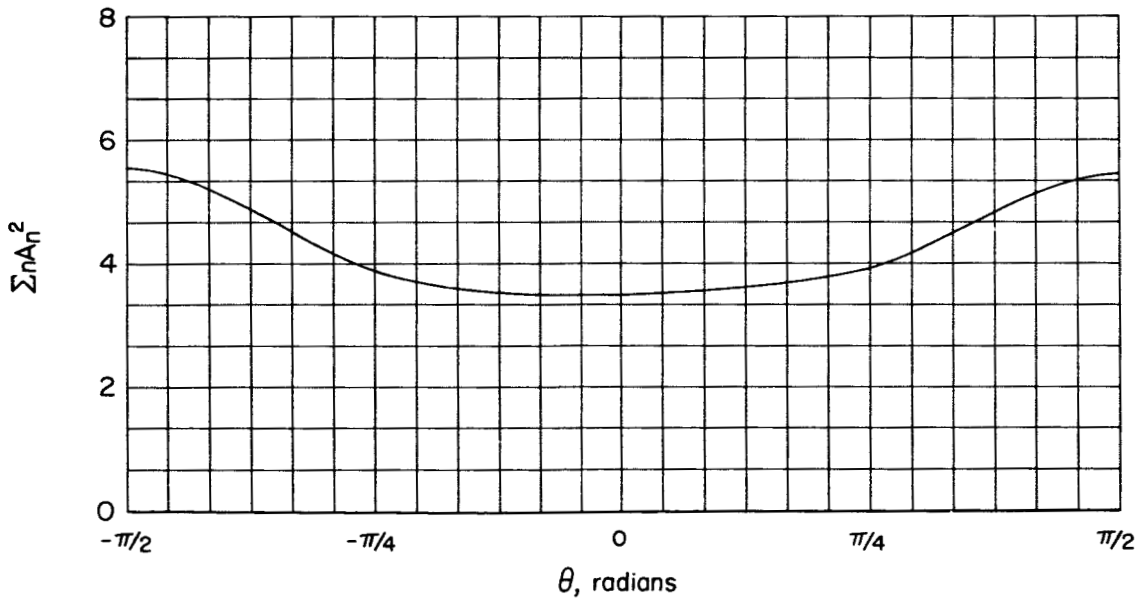
(b) $\Sigma n A_n^2$ vs. θ

Figure 3.- Area distributions and a quantity proportional to the zero-lift wave drag for equivalent bodies of model F less tail at a Mach number of 1.5.

C_{D_0}

.4

.3

.2

.1

0

Experiment: R = 5.3 x 10⁶ ————
to 10 x 10⁶ per ft

Friction drag plus afterbody, —— —— ——
fin, and base pressure drag

ΔC_{D_0}

(a) C_{D_0} vs. M

ΔC_{D_0}

.2

.1

0

Experiment less friction drag, less —————
afterbody, fin, and base pressure drag

Theory, N = 24 (ref. 2) ———————

0   .2   .4   .6   .8   1.0   1.2   1.4   1.6   1.8   2.0

M

(b) ΔC_{D_0} vs. M
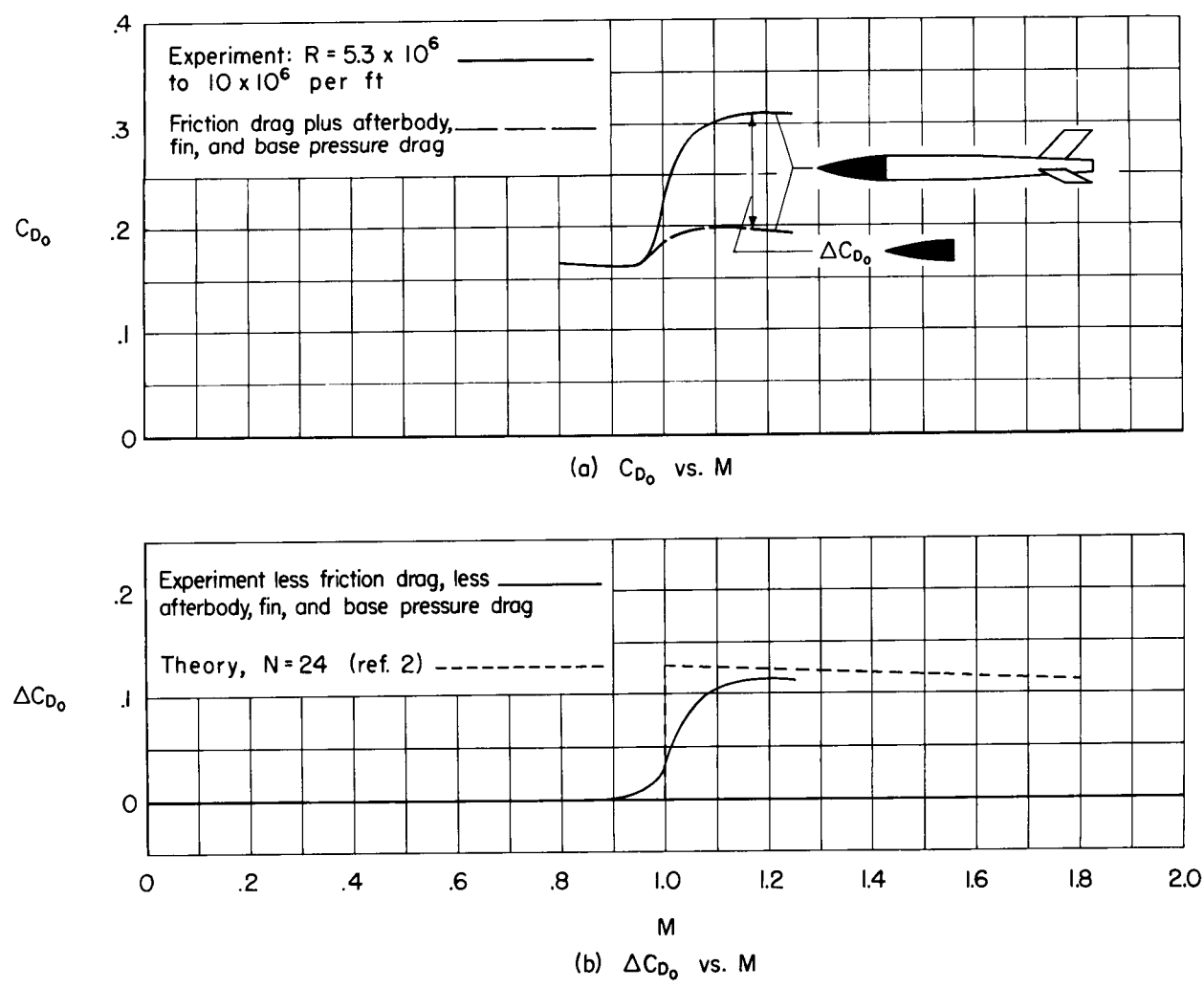
Figure 4.- Comparison of experimental and theoretical zero-lift wave-drag coefficients; model A.

(a) C_{D_o} vs. M

(b) ΔC_{D_o} vs. M
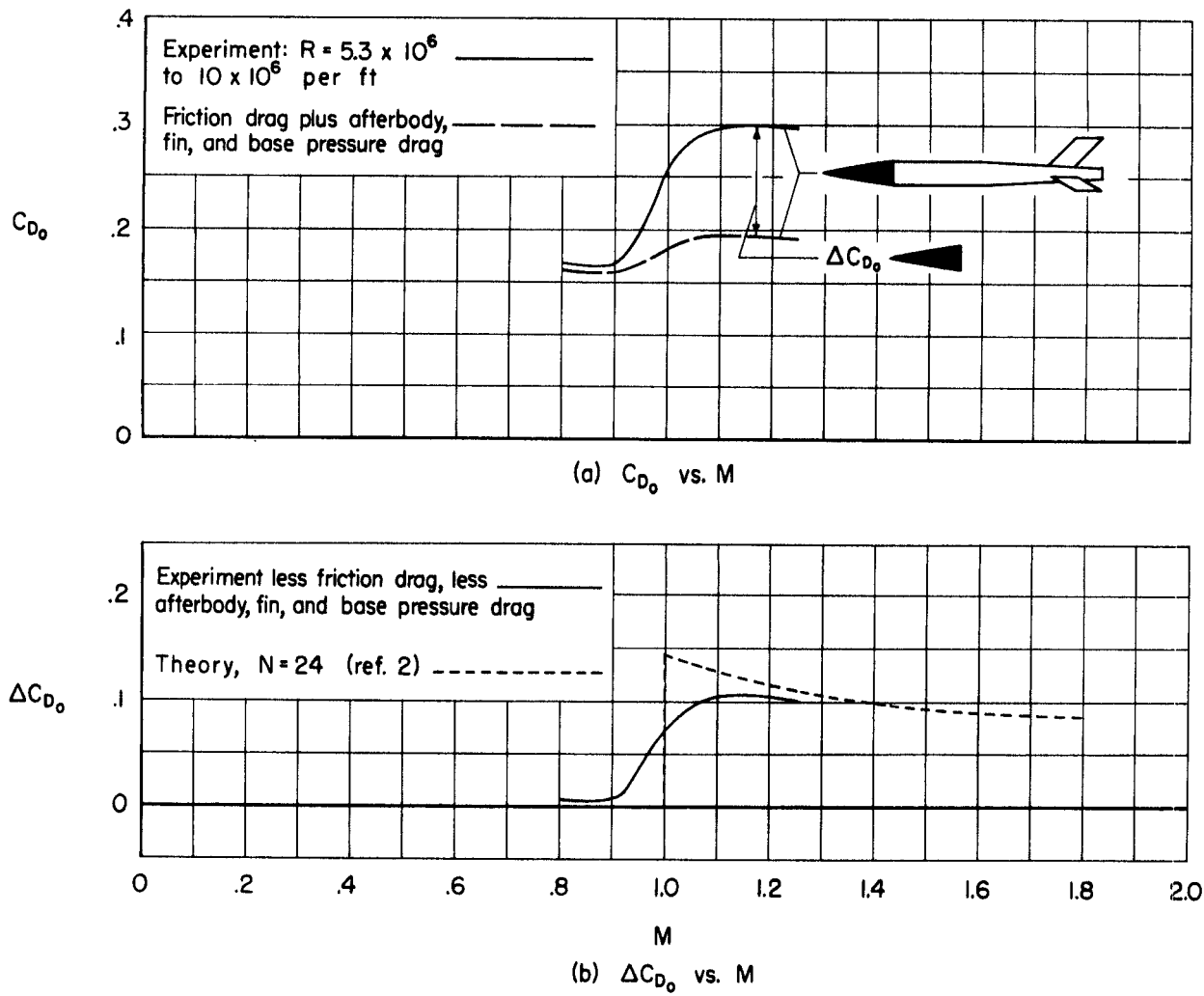
Figure 5.- Comparison of experimental and theoretical zero-lift wave-drag coefficients; model B.

(a) C_{D_0} vs. M

(b) C_{D_0} vs. M
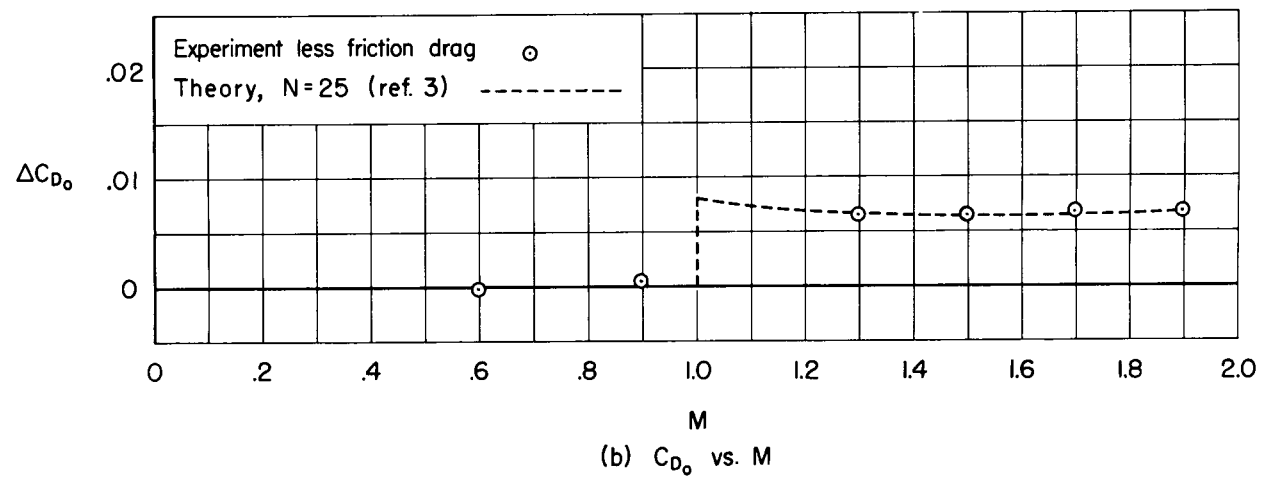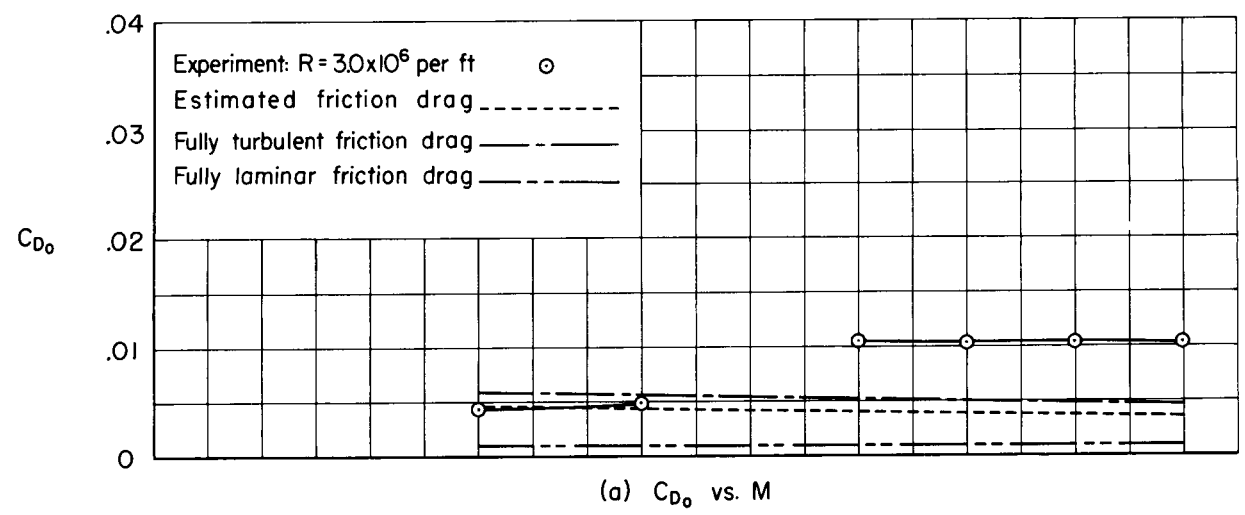
Figure 6.- Comparison of experimental and theoretical zero-lift wave-drag coefficients; model C.

(a) C_{D_0} vs. M

(b) ΔC_{D_0} vs. M
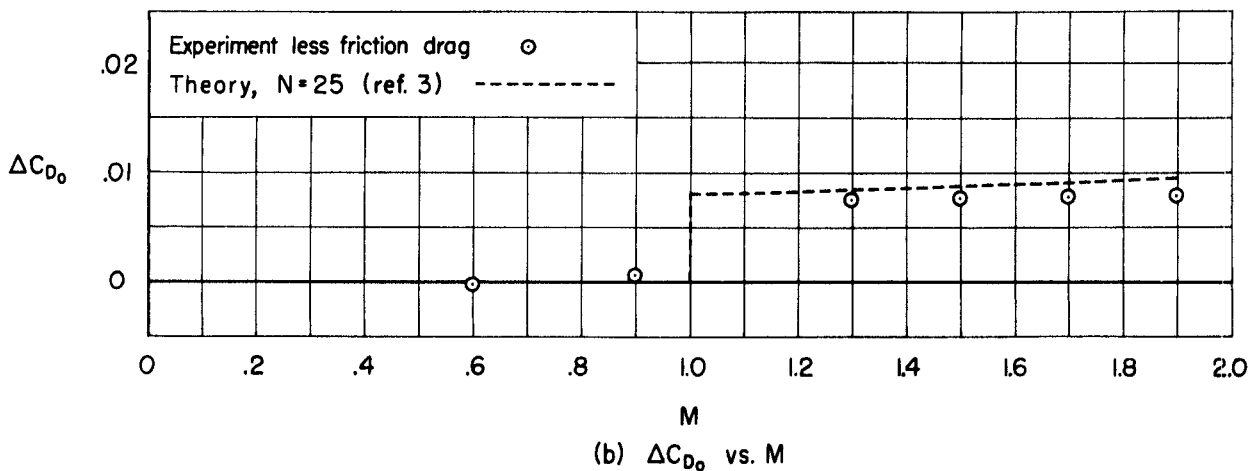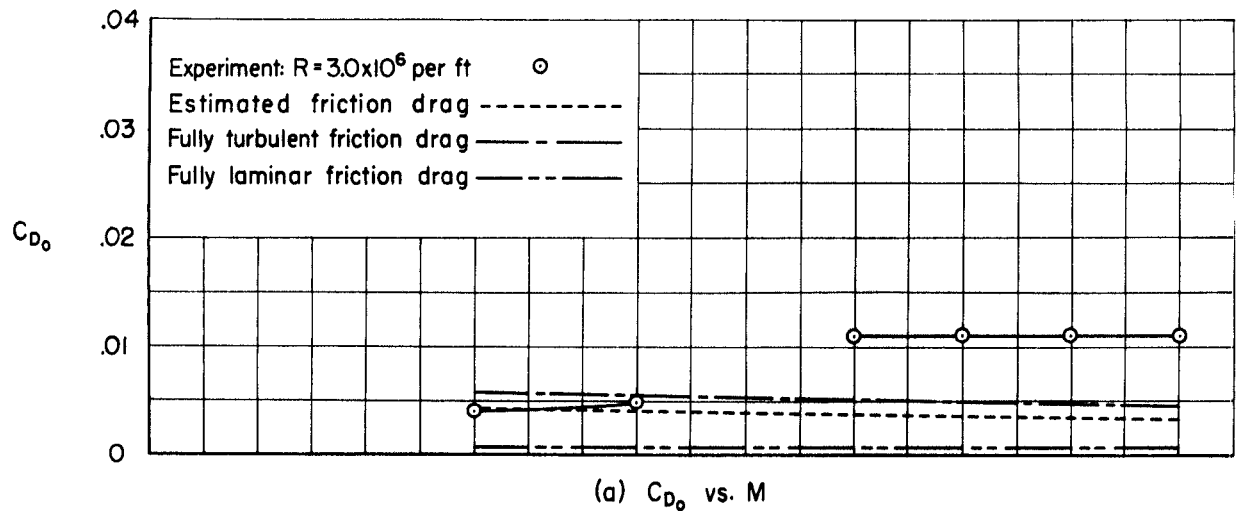
Figure 7.- Comparison of experimental and theoretical zero-lift wave-drag coefficients; model D.
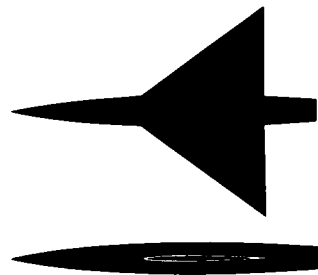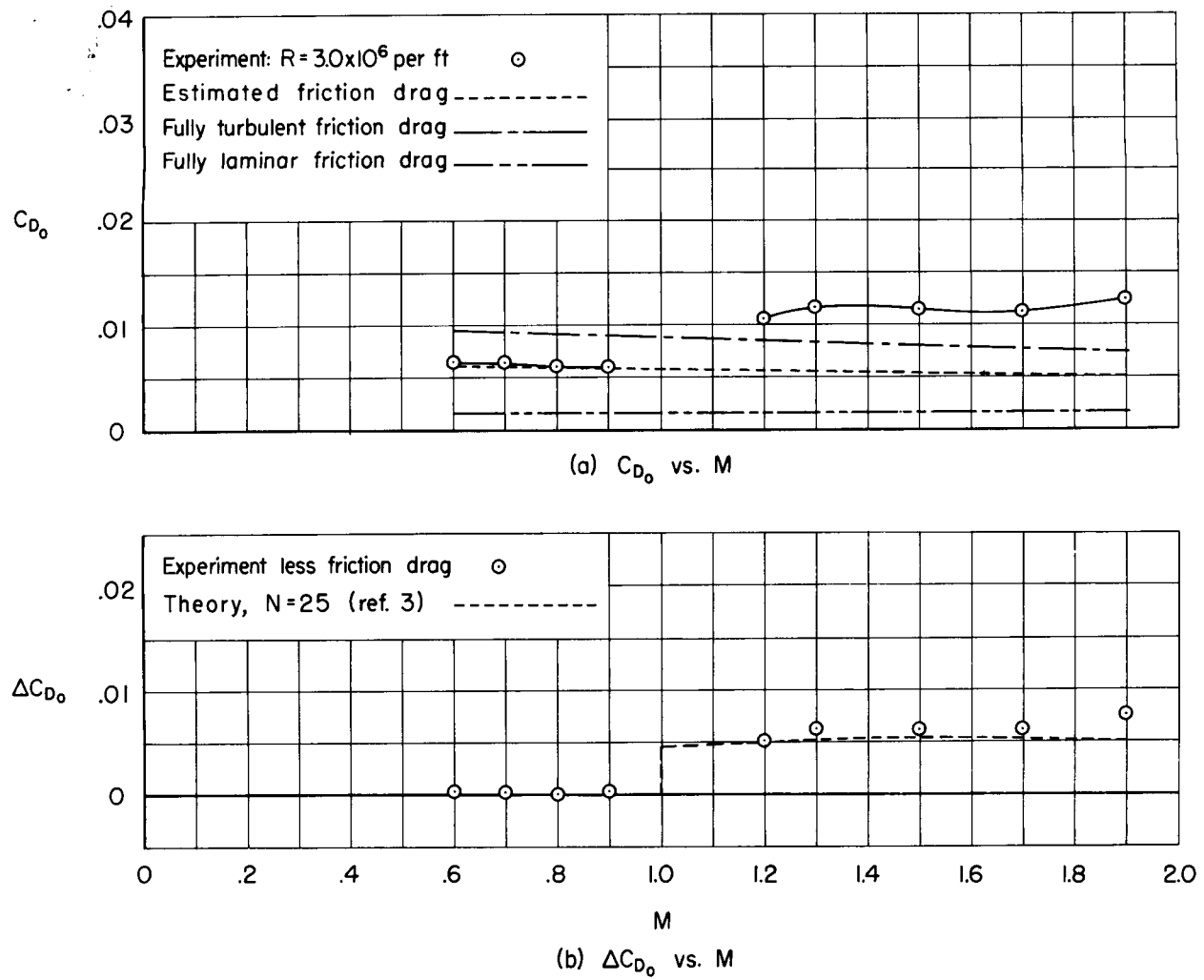
(a) C_{D_0} vs. M

(b) ΔC_{D_0} vs. M

Figure 8.- Comparison of experimental and theoretical zero-lift wave-drag coefficients; model E.
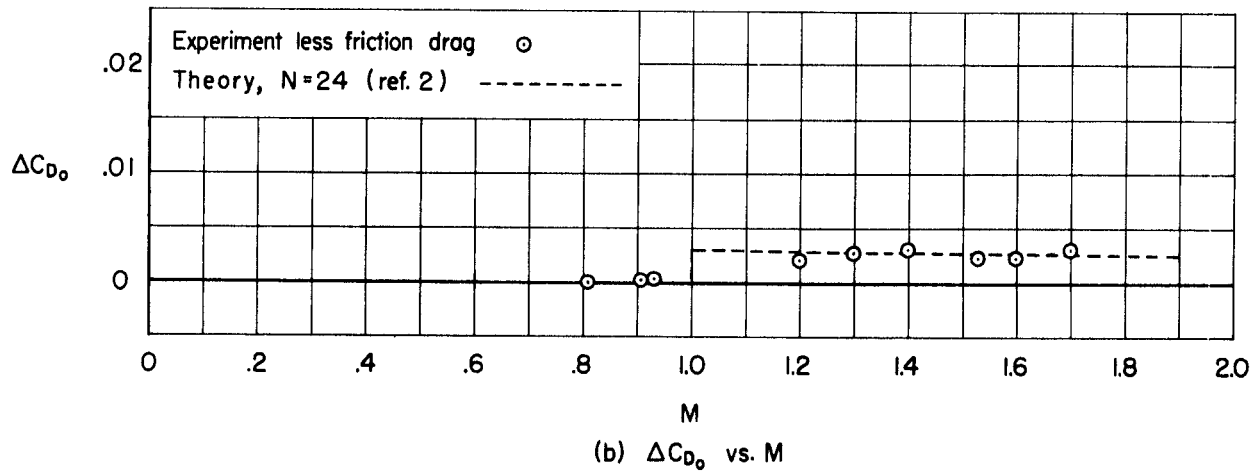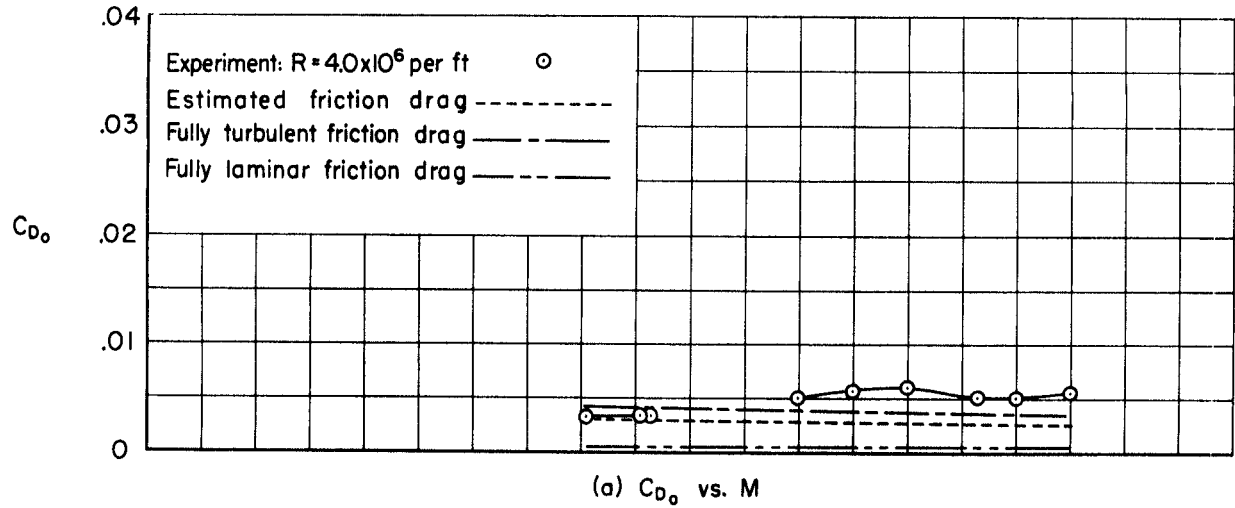
(a) C_{D_0} vs. M

(b) ΔC_{D_0} vs. M

Figure 9.- Comparison of experimental and theoretical zero-lift wave-drag coefficients; model E less wing.
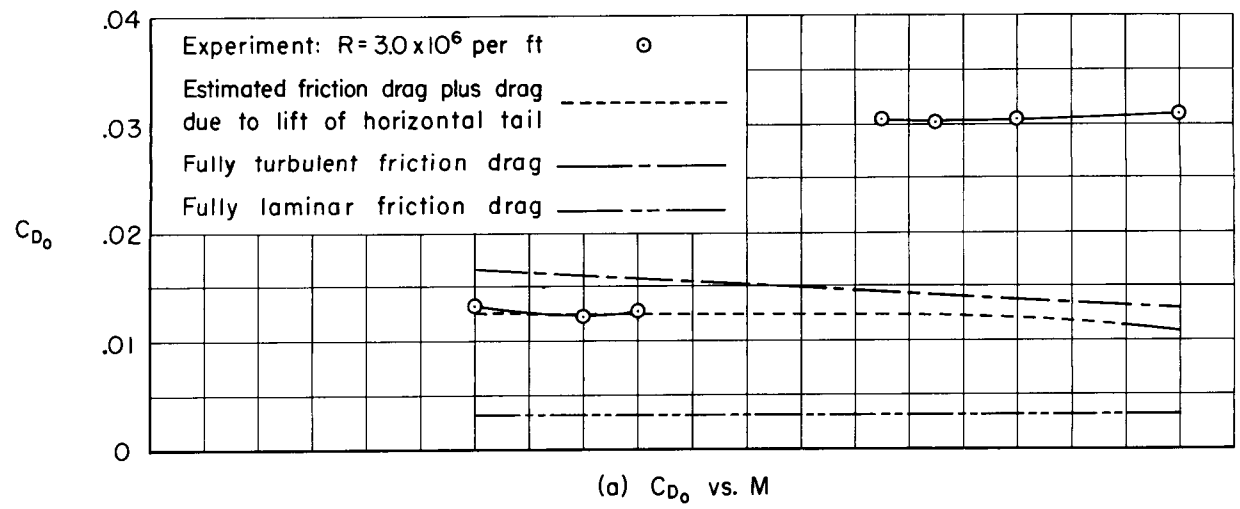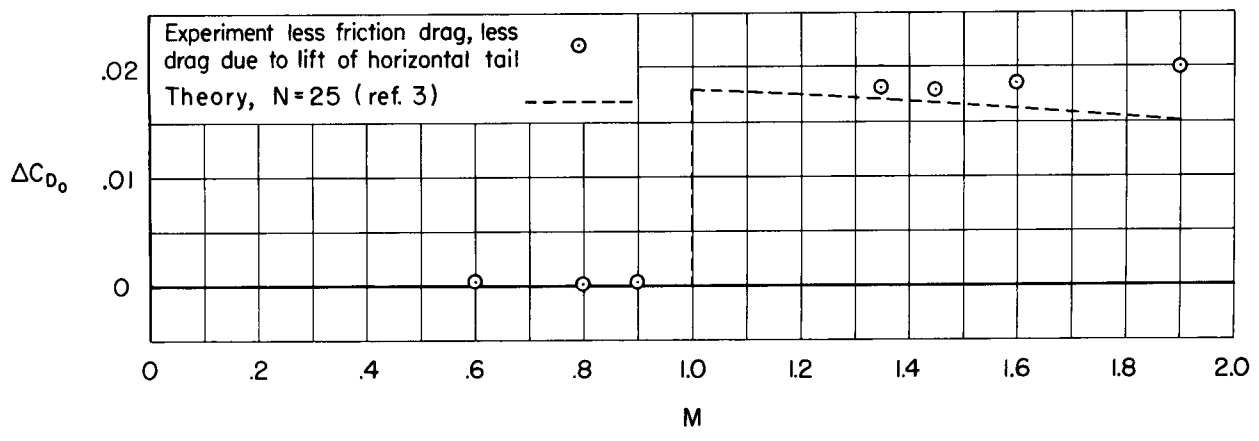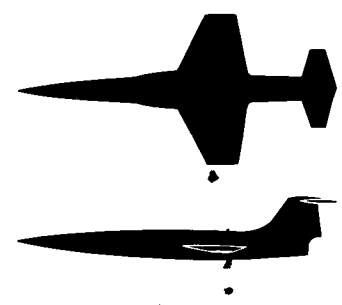
Figure 10.- Comparison of experimental and theoretical zero-lift wave-drag coefficients; model F.
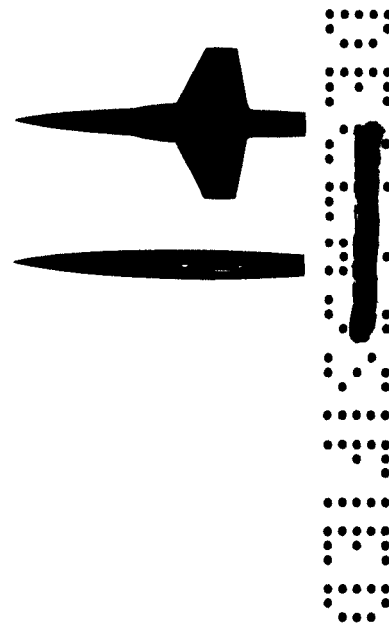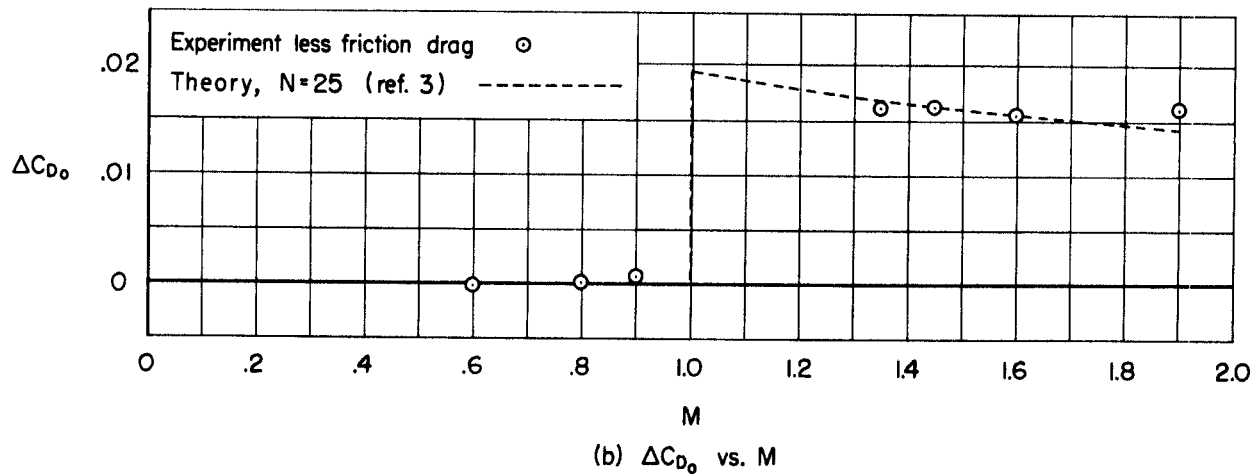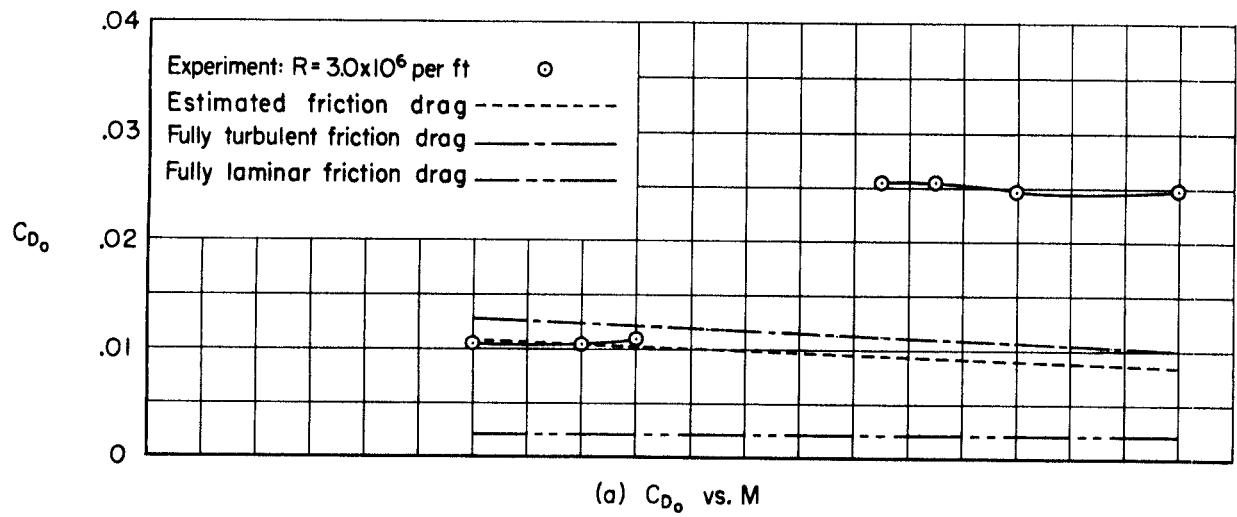
(a) C_{D_0} vs. M

(b) ΔC_{D_0} vs. M

Figure 11.- Comparison of experimental and theoretical zero-lift wave-drag coefficients; model F less tail.
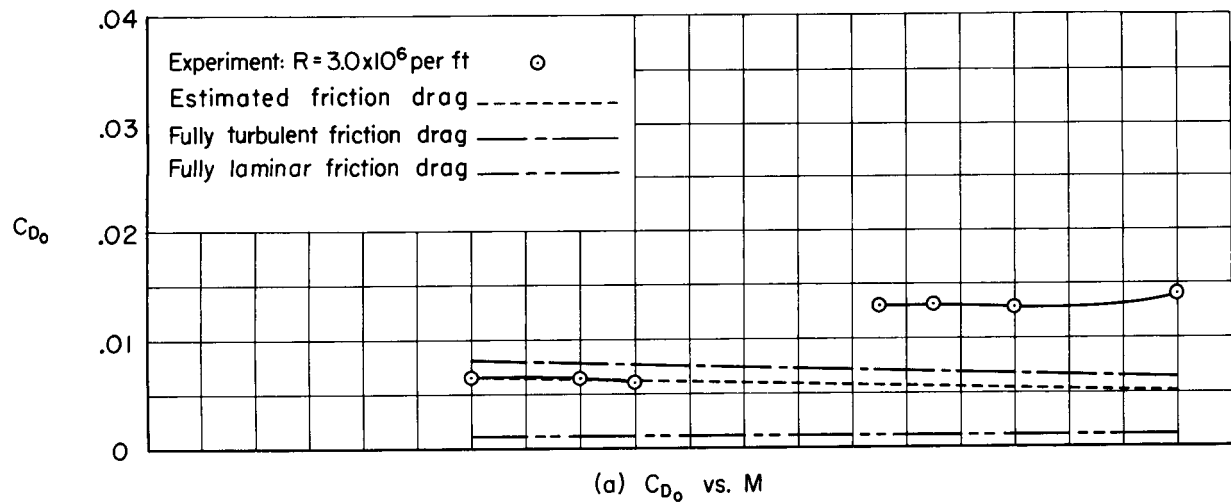
(a) C_{D_0} vs. M
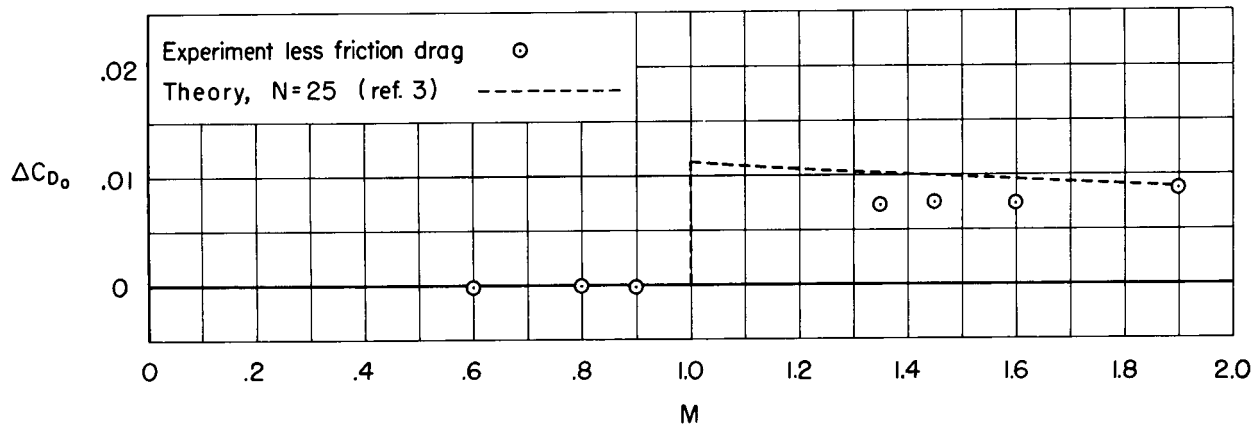
(b) ΔC_{D_0} vs. M

Figure 12.- Comparison of experimental and theoretical zero-lift wave-drag coefficients; model F less wing, tail, and ducts.
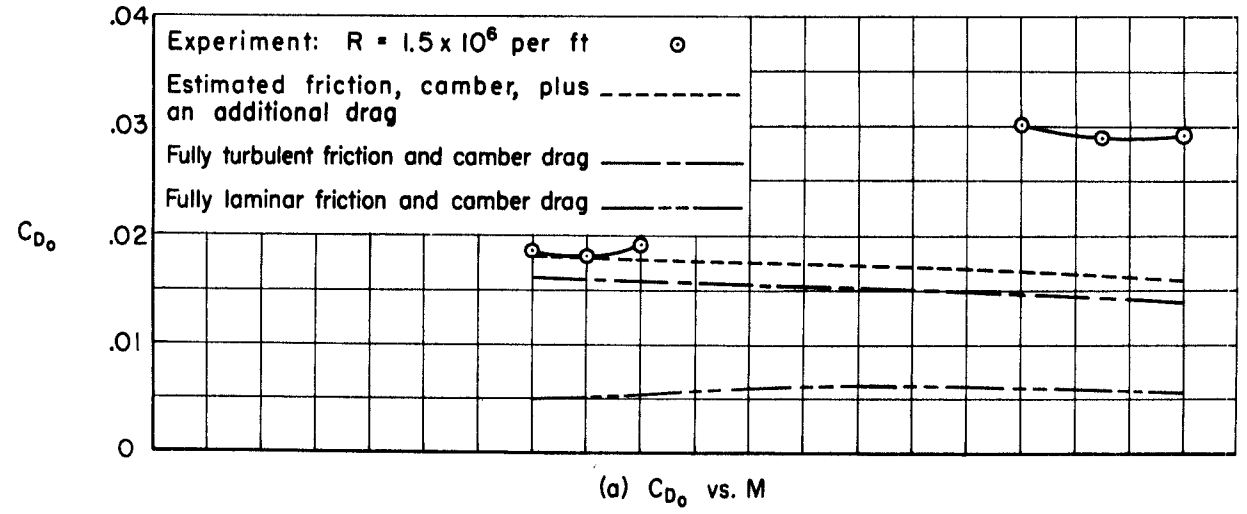
(a) C_{D_0} vs. M
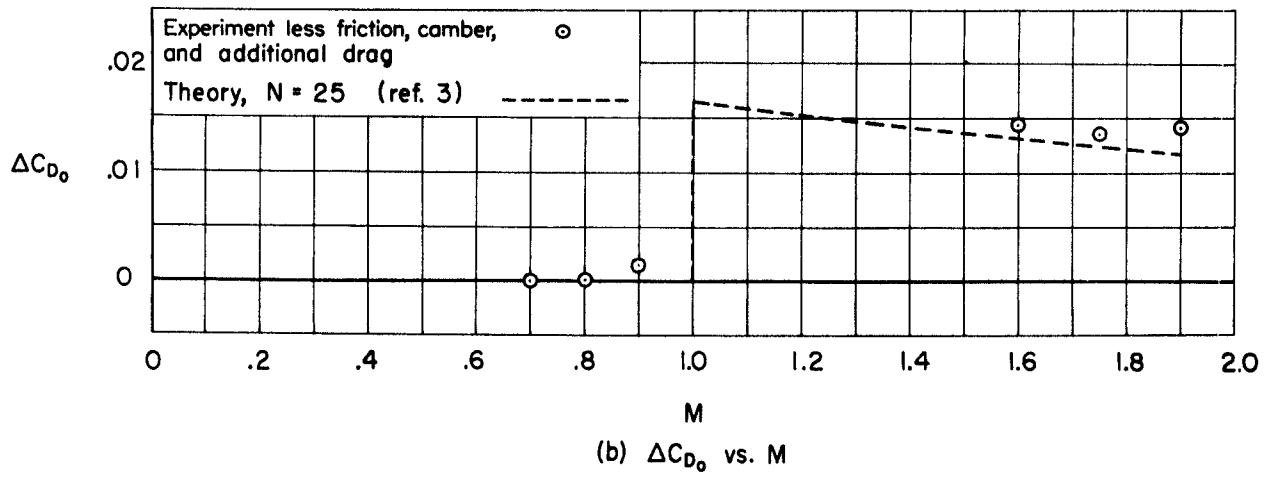
(b) ΔC_{D_0} vs. M

Figure 13.- Comparison of experimental and theoretical zero-lift wave-drag coefficients; model G.
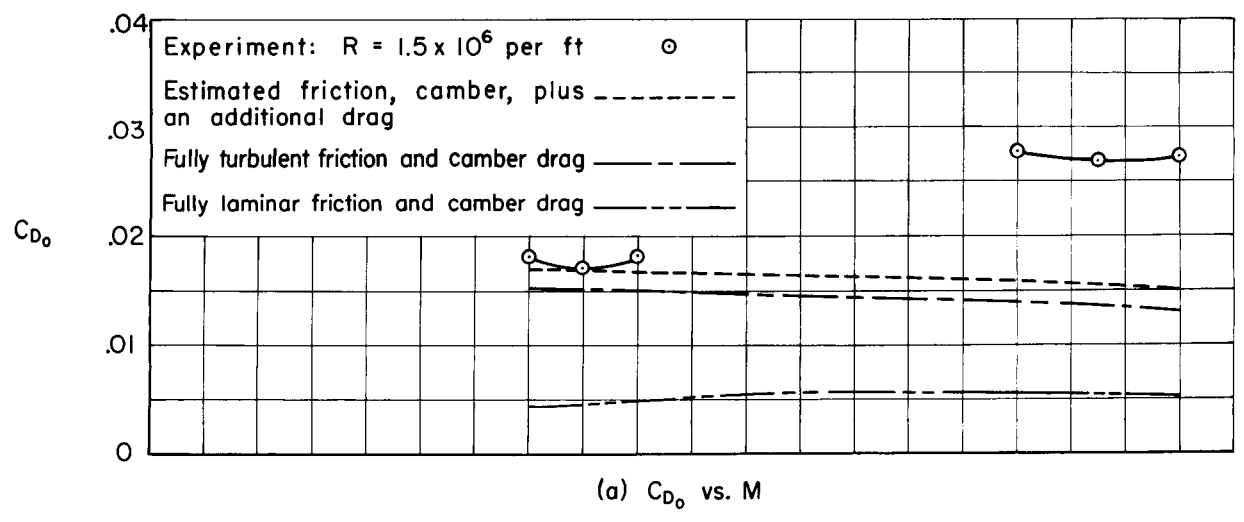
(a) C_{D_0} vs. M
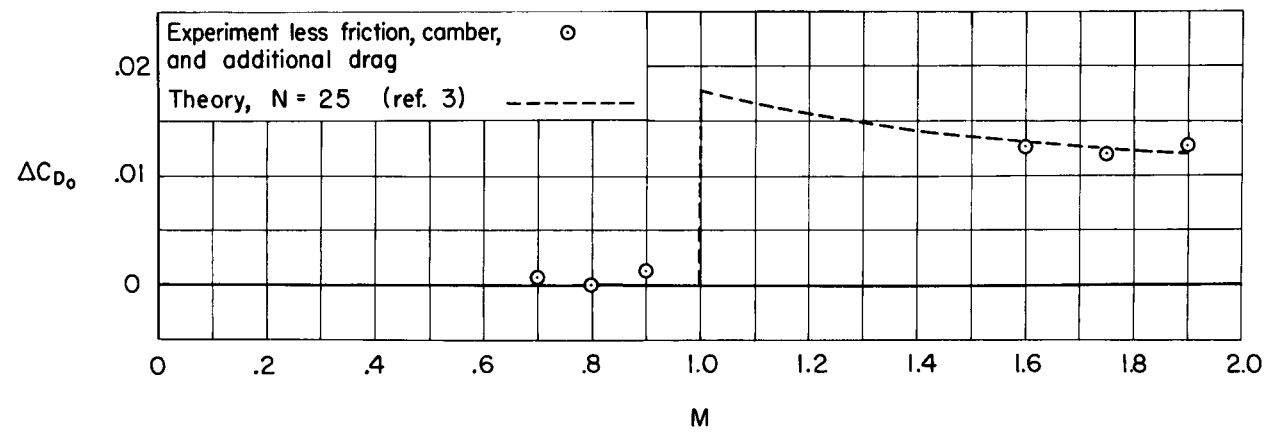
(b) ΔC_{D_0} vs. M

Figure 14.- Comparison of experimental and theoretical zero-lift wave-drag coefficients; model G less tail.
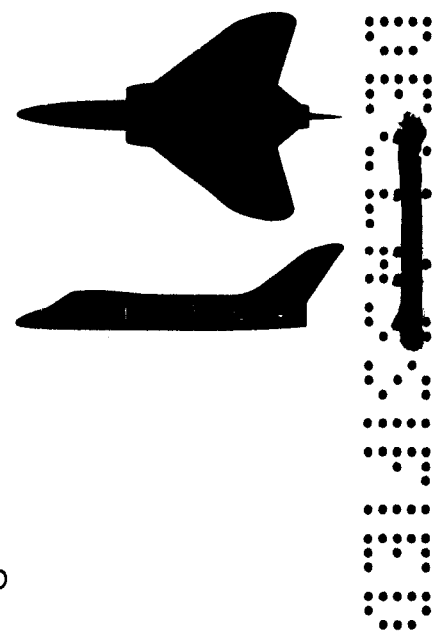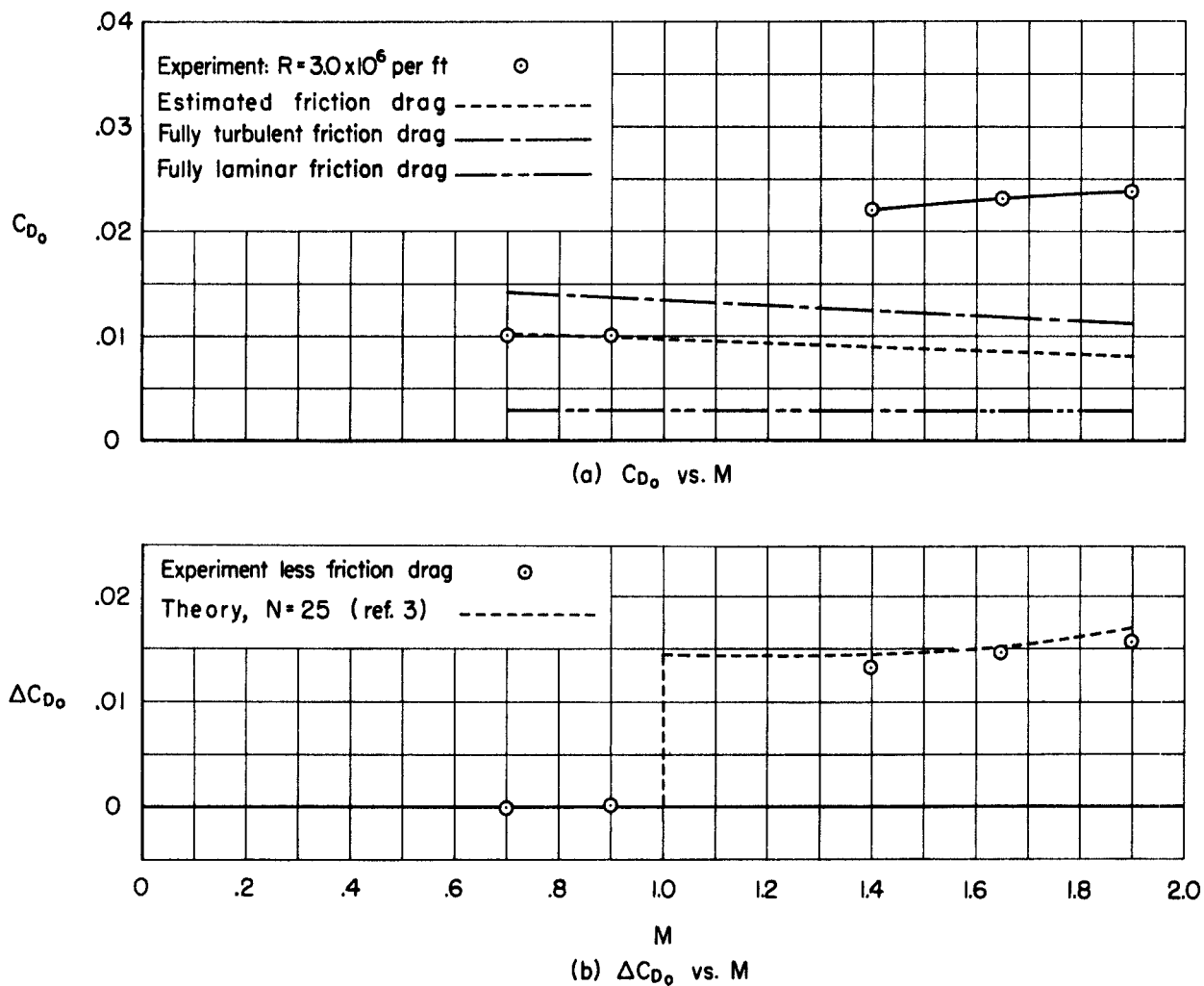
Figure 15.- Comparison of experimental and theoretical zero-lift wave-drag coefficients; model H.

(a) C_{D_o} vs. M
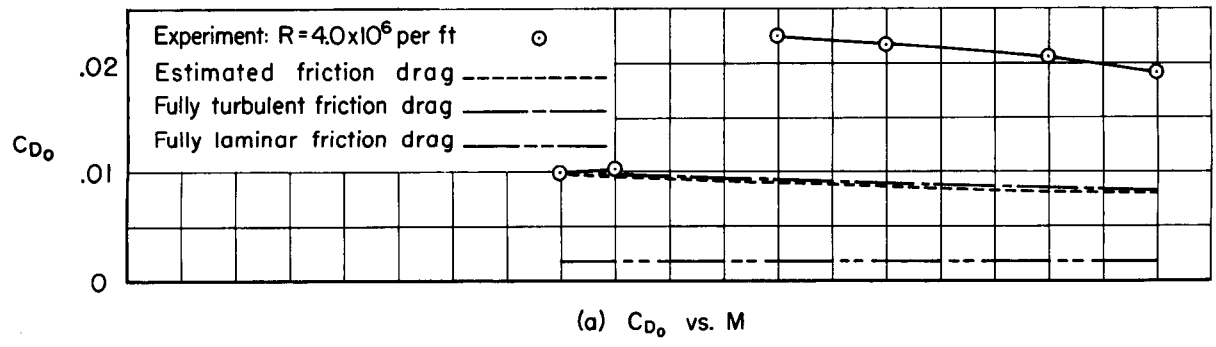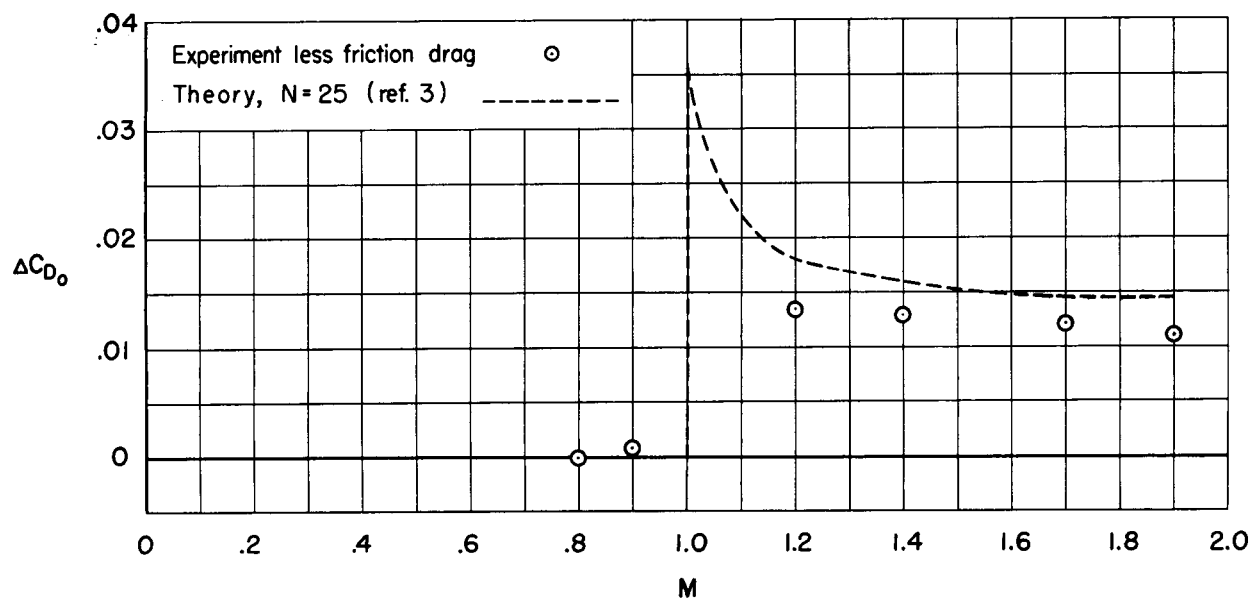
(b) ΔC_{D_o} vs. M

Figure 16.- Comparison of experimental and theoretical zero-lift wave-drag coefficients; model I.
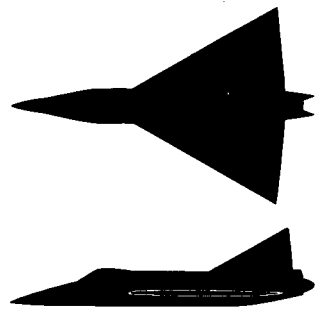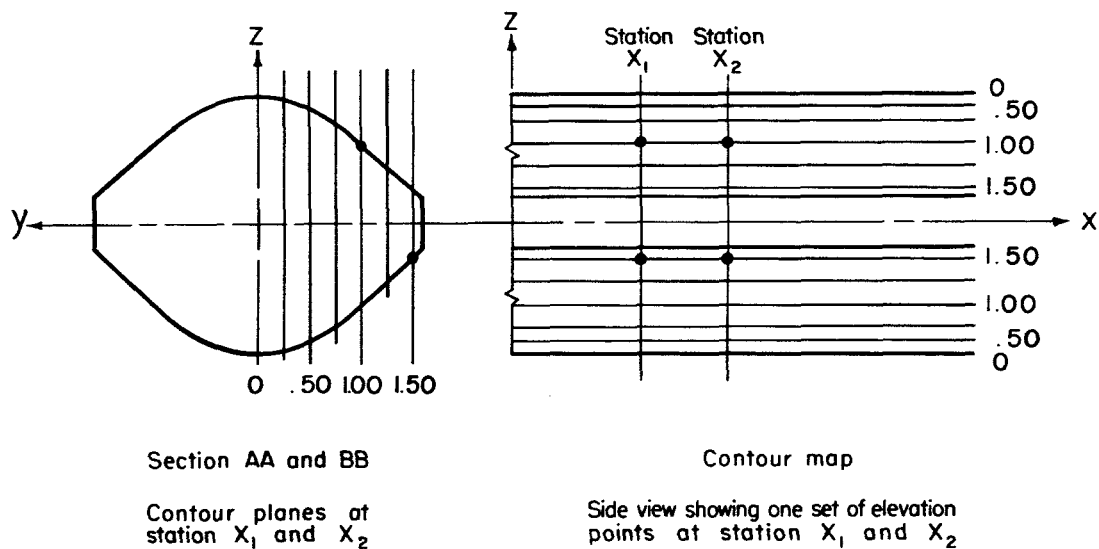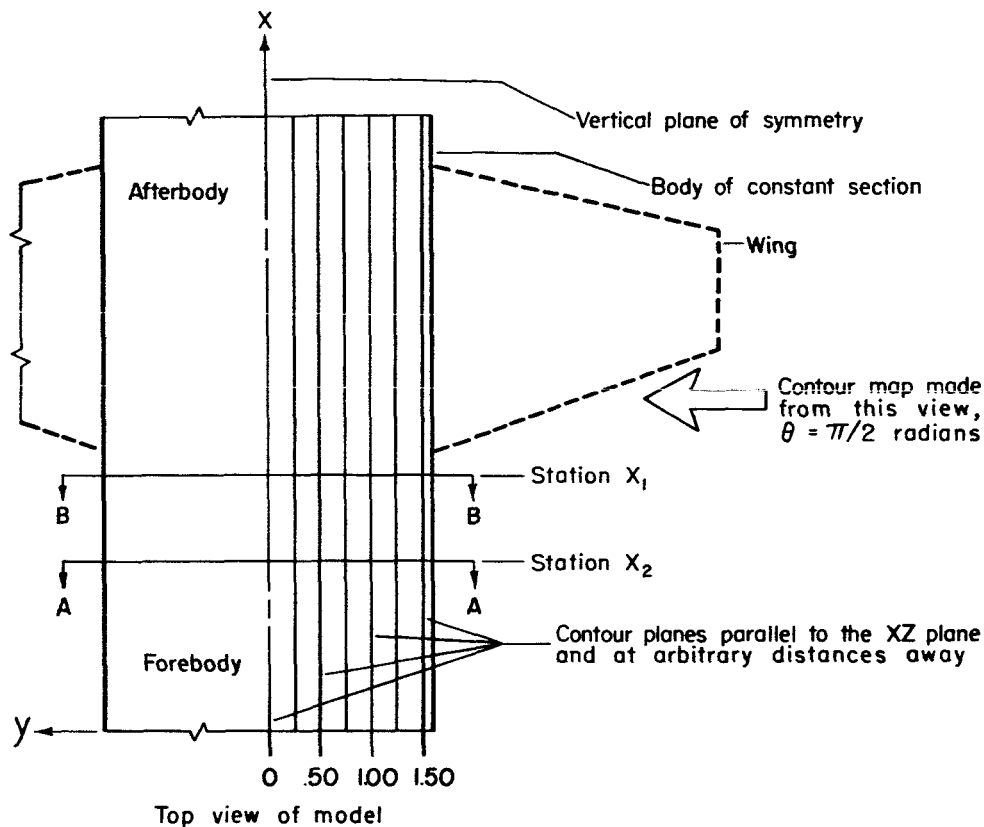
(a) Construction of a contour map.

Figure 17.- Graphical layout for determining area distribution of a body.
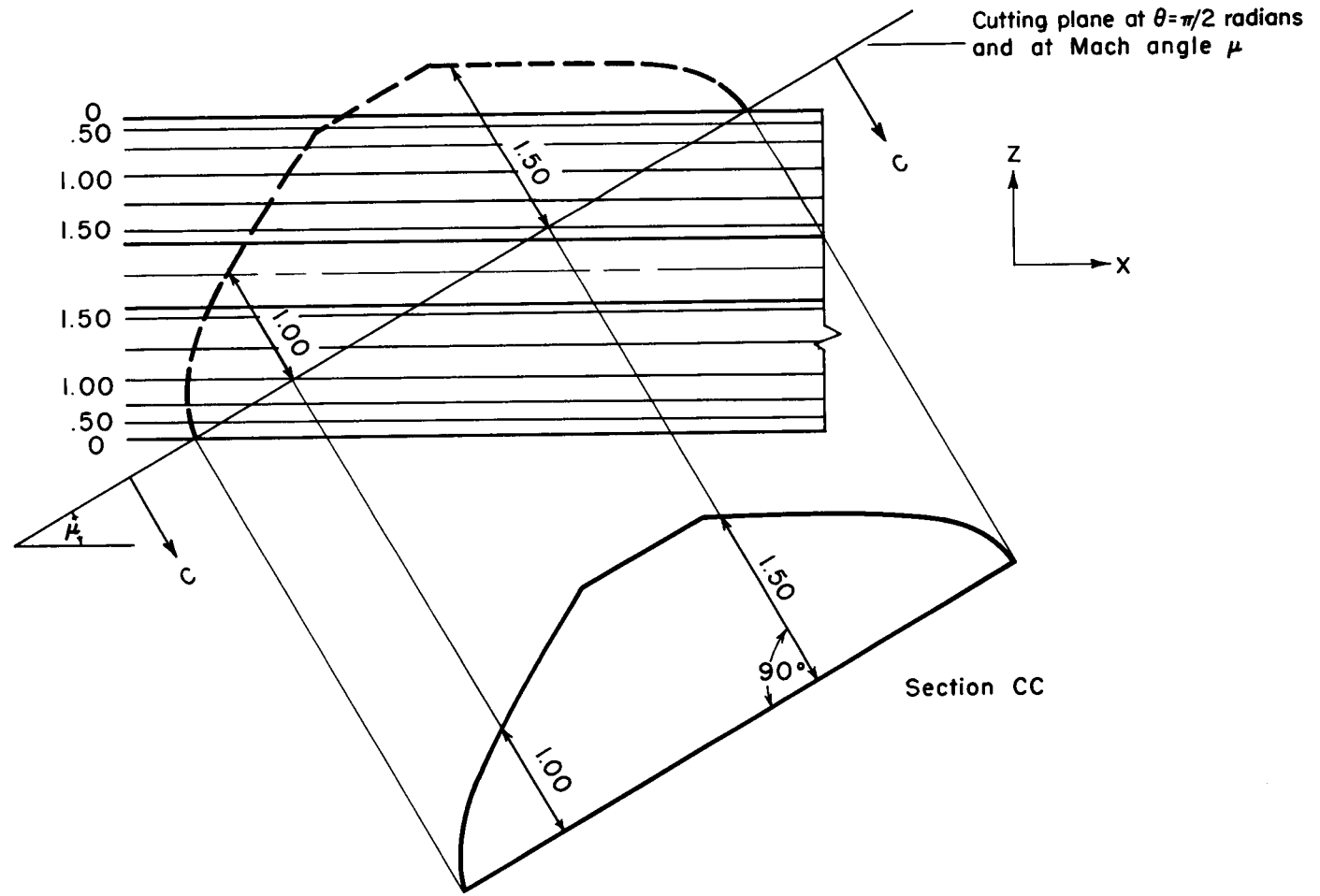
(b) Contour map of side view (figure 17(a)) and area cut at a roll angle of $\theta = \pi/2$ and Mach angle μ.

Figure 17.- Continued.
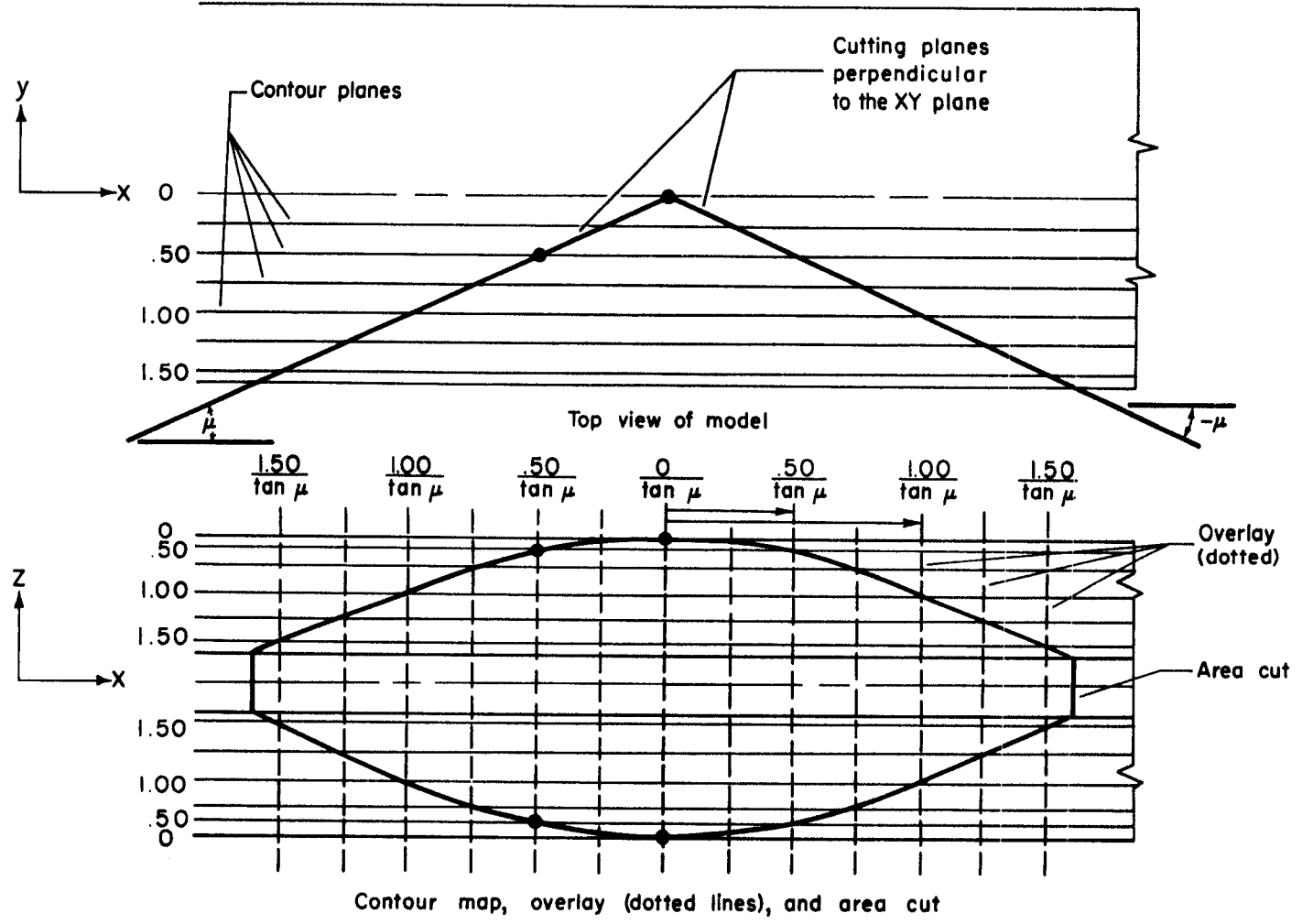
(c) Top view of model and contour map of side view with area cut at roll angle $\theta = 0$.

Figure 17.- Concluded.

Wing chord plane

Wing surface

Note: Symmetrical airfoil section

Ordinate of wing

Typical sections cut
by oblique planes

Ordinate rotated until
perpendicular to cutting planes

90°

90°

Body—wing juncture

r

r

Ψ

Ψ

Reference body axis

Station positions of area
cut by oblique planes
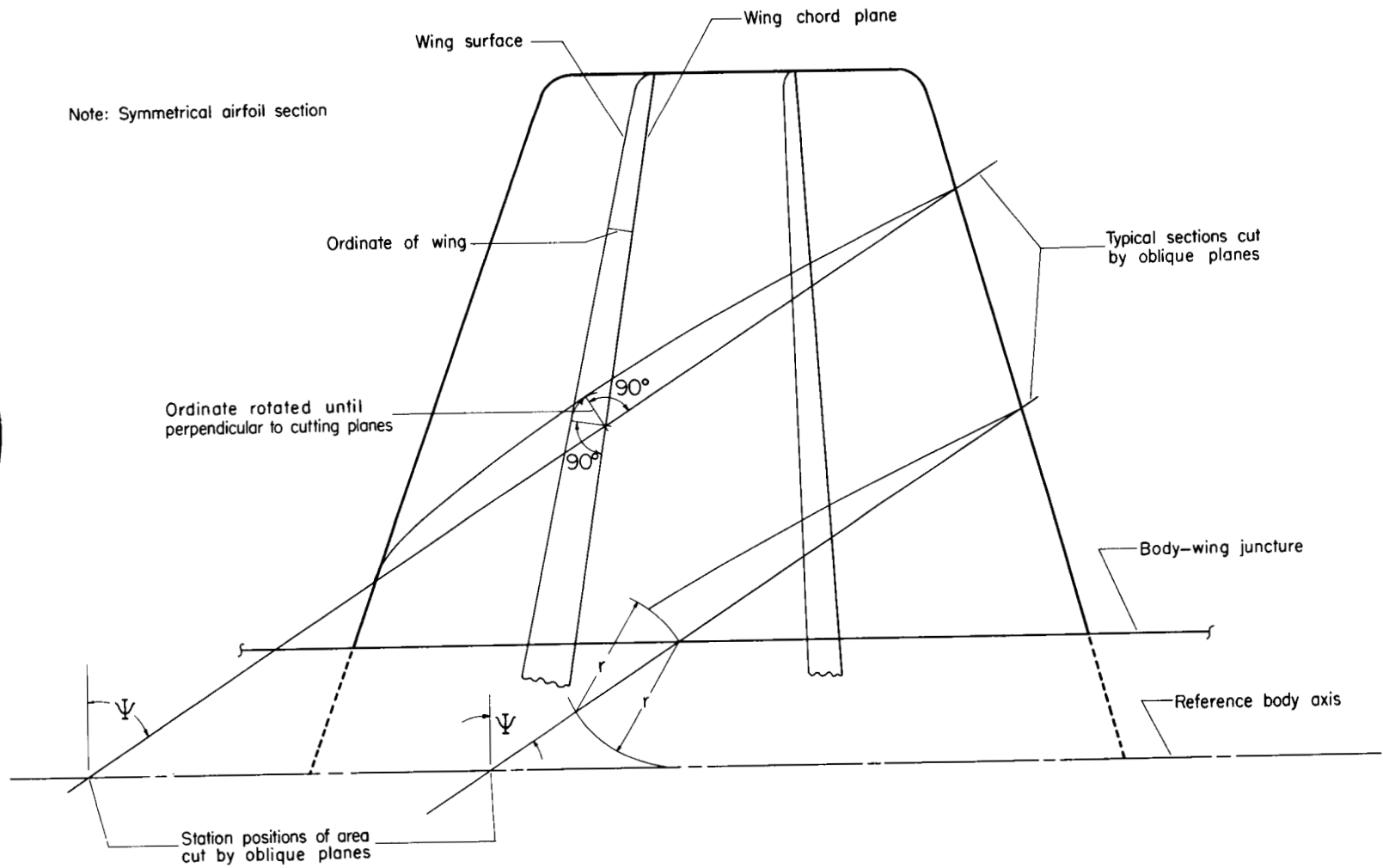
Figure 18.- Graphical layout for determining area distribution of a wing.